Microglia facilitate and stabilize the response to general anesthesia

Yang He[1,#], Taohui Liu[1,#], Quansheng He[1,#], Wei Ke[1], Xiaoyu Li[1], Jinjin Du[1,2], Suixin Deng[1], Zhenfeng Shu[1], Jialin Wu[1], Baozhi Yang[1,2], Yuqing Wang[1,2], Ying Mao[1], Yanxia Rao[3], Yousheng Shu[1,*] and Bo Peng[1,4,*]

1 Department of Neurosurgery, Huashan Hospital, Institute for Translational Brain Research, State Key Laboratory of Medical Neurobiology, MOE Frontiers Center for Brain Science, Innovative Center for New Drug Development of Immune Inflammatory Diseases, Ministry of Education, Fudan University, Shanghai 200040, China.
2 School of Basic Medical Sciences, Jinzhou Medical University, Jinzhou, Liaoning 121001, China.
3 Department of Neurology, Zhongshan Hospital, Department of Laboratory Animal Science, MOE Frontiers Center for Brain Science, Fudan University, Shanghai 200032, China.
4 Co-Innovation Center of Neurodegeneration, Nantong University, Nantong, Jiangsu 226001, China.
Co-first authors
* Corresponding authors

Correspondence should be addressed to:
Dr. Yousheng Shu
Fudan University, Shanghai, China.
E-mail: yousheng@fudan.edu.cn

Dr. Bo Peng
Fudan University, Shanghai, China.
E-mail: peng@fudan.edu.cn

Number of figures: 14

Abstract

General anesthesia leads to a loss of consciousness and an unarousable state in patients. Although general anesthetics are widely used in clinical practice, their underlying mechanisms remain elusive. The potential involvement of nonneuronal cells is unknown. Microglia are important immune cells in the central nervous system (CNS) that play critical roles in CNS function and dysfunction. We unintentionally observed delayed anesthesia induction and early anesthesia emergence in microglia-depleted mice. We found that microglial depletion differentially regulates neuronal activities by suppressing the neuronal network of anesthesia-activated brain regions and activating emergence-activated brain regions. Thus, microglia facilitate and stabilize the anesthesia status. This influence is not mediated by dendritic spine plasticity. Instead, it relies on the activation of microglial P2Y12 and subsequent calcium influx, which facilitates the general anesthesia response. Together, we elucidate the regulatory role of microglia in general anesthesia, extending our knowledge of how nonneuronal cells modulate neuronal activities.

Introduction

General anesthesia is a cornerstone of modern medical sciences. Upon the use of anesthetics, patients lose consciousness and enter an unarousable state. Although general anesthetics are widely used in clinical procedures, the mechanism of general anesthesia remains elusive. Different anesthetics activate or inhibit specific receptors in neurons, modulating neuronal activities across the entire network. However, the involvement of nonelectrically active glial cells in anesthesia is poorly understood. Microglia are yolk sac-derived glial cells in the central nervous system (CNS) (1). They play critical roles in CNS development, function and dysfunction (2, 3). Previous studies have found that neuronal activity in the CNS network modulates microglial activity. Microglia exhibit elevated process motility, extension and territory surveillance during anesthetization and sleep (4, 5). Suppression of neuronal activity increases calcium signaling in microglial processes (6). Conversely, microglia also modulate neuronal activity via multiple mechanisms (7-12). The microglial regulation of neuronal activities thus raises the question of whether microglia can modulate the general anesthesia response.

Microglial survival relies on colony-stimulating factor 1 receptor (CSF1R) signaling (13). Pharmacological inhibition of CSF1R efficiently eliminates CNS microglia (14-19). Previous studies have shown that acute microglial depletion does not induce neuroinflammation (14, 15, 19, 20). The ablation of microglia in adulthood also does not result in obvious general behavioral dysfunctions (14, 20), although this finding is controversial (21). It seems that microglia are disposable under physiological conditions. However, when we killed microglia with PLX5622, a CSF1R inhibitor (22), we unintentionally observed robust resistance to anesthetic administration. This suggests that microglia may facilitate general anesthesia by modulating neuronal network activity.

To this end, we first quantified the influence of microglial depletion on the response to general anesthesia. We utilized the loss of righting reflex (LORR) and recovery of righting reflex (RORR) to evaluate anesthesia induction and emergence, respectively. After microglial depletion, mice displayed a longer LORR time and a shorter RORR time. The dampened general anesthesia response was not dependent on specific anesthetics or receptors, as this phenomenon was observed with three different agonists of the $GAGA_A$ receptor (pentobarbital, propofol and chloral hydrate) and one antagonist of the NMDA receptor (ketamine). Electroencephalography (EEG) and electromyography (EMG) findings further confirmed our initial observation. Different brain regions diversely regulate anesthesia induction and emergence. Anesthesia induction is positively correlated with anesthesia-activated brain regions (AABRs). In contrast, anesthesia emergence is positively correlated with emergence-activated brain regions (EABRs). We observed that microglia modulate brain network activity in a brain region-specific manner rather than in a universal manner for all brain regions. Based on c-Fos reactivity and patch clamp recordings, we demonstrated that microglial depletion inhibits AABRs and activates EABRs. The divergent effects in different brain regions orchestrate the status during general anesthesia use. Microglia-mediated anesthesia modulation is not attributed to dendritic spine plasticity. We found that mice with genetical knockout or pharmacological inhibition of microglial P2Y12 were more resistant to general anesthesia. In addition, the contribution of microglial P2Y12 to anesthesia response was further confirmed by the mice received microglia replacement, in which the replaced microglia-like cells are $P2Y12^{-}$ (18). On the other hand, the intracellular Ca^{2+} concentration in microglia facilitates and stabilizes the response to general anesthesia. Because purinergic activation of P2Y12 increases intracellular Ca^{2+} (23-25), our results reveal that the general anesthesia response is regulated through P2Y12 to Ca^{2+} signaling in microglia.

In conclusion, our study demonstrates a regulatory role of microglia in the response to general anesthesia and identifies the underlying mechanism of this process. This study extends our knowledge of how nonelectrically active glial cells regulate the general

anesthesia response. It also sheds new light on how microglia contribute to maintaining the status of the brain network. When we were preparing our manuscript, a paper discussing a similar topic emerged (26).

Results

Microglia regulate the induction of and emergence from general anesthesia

We unintentionally observed that mice become more resistant to anesthesia after microglia and macrophage depletion by the CSF1R inhibitor PLX5622. To quantitatively study whether microglial depletion indeed influences the induction of and emergence from general anesthesia, we first fed mice a PLX5622-formulated diet (PLX5622 hereafter) to ablate CNS microglia and peripheral macrophages (16, 18, 19, 27). After 14 days of PLX5622 administration, we intraperitoneally injected pentobarbital (80 mg pentobarbital sodium per kg of body weight) into the PLX5622-treated mice (Figure 1A). Compared to naïve mice on day 0 (D0), the PLX5622-treated mice at D14 displayed a longer time for LORR and shorter time for RORR (Figure 1B). Pentobarbital is an agonist of the $GABA_A$ receptor (28). We next examined whether this microglia- and macrophage-mediated regulation of the anesthesia response is restricted to pentobarbital or $GABA_A$ receptor agonists. We assessed LORR and RORR in PLX5622-treated mice by using other anesthetics, including two other $GABA_A$ receptor agonists (propofol, 200 mg/kg of body weight; chloral hydrate, 400 mg/kg of body weight) (29-31) and one NMDA receptor antagonist (ketamine, 100 mg/kg of body weight) (32). Similar trends were observed in propofol-, chloral hydrate- and ketamine-induced LORR and RORR (Figure 1B). To exclude the possibility that PLX5622-induced anesthesia resistance results from tolerance to repetitive anesthetic injection, we sequentially treated mice with the same anesthetics 5 times at 7-day intervals (Figure 2A). Both LORR and RORR were unchanged for pentobarbital, propofol, chloral hydrate and ketamine, except for chloral hydrate-induced LORR after D14 (the third dose) (Figure 2B). PLX5622-treated mice exhibited a resistant phenotype (Figure 1B). In contrast, the third dose of chloral hydrate made mice more susceptible to anesthesia (Figure 2B), an opposite trend from PLX5622 treatment. Consequently, PLX5622-induced anesthesia resistance is not attributed to the tolerance of repetitive anesthetic administration.

PLX5622 can simultaneously ablate brain microglia and peripheral macrophages (27). To exclude the possibility that CSF1R-mediated general anesthesia regulation does not result from peripheral macrophages, we utilized the blood-brain barrier-impermeable CSF1R inhibitor PLX73086 to ablate peripheral macrophages without influencing brain microglia (33). After administration of the PLX73086-formulated diet (PLX73086 hereafter) for 14 days, macrophages in the liver, lung, spleen and kidney were significantly ablated, while brain microglia were not influenced (Figure 3A-B). PLX73086-treated mice (peripheral macrophage-depleted, brain microglia-unchanged) displayed similar general anesthetic responses as CD-treated naïve mice, including those treated with pentobarbital, propofol, chloral hydrate and ketamine, except for the RORR in pentobarbital-treated mice (Figure 3C). Since PLX73086-treated mice (peripheral macrophage-depleted, brain microglia-unchanged) exhibited a delayed RORR with pentobarbital administration (Figure 3C), whereas PLX5622-treated mice (peripheral macrophage-depleted, brain microglia-depleted) displayed an earlier RORR (Figure 1B), the pentobarbital-induced early emergence in PLX5622-administered mice is not attributed to peripheral macrophage ablation. Therefore, microglial depletion, rather than macrophage depletion, leads to resistance to general anesthesia.

Next, we reasoned whether this anesthesia resistance is permanent or can be reversed by microglial repopulation. To address this question, we ceased CSF1R inhibition by treating the microglia-depleted mice with a control diet (CD) for 21 days to allow microglia to repopulate the brain (Figure 1A), at which point repopulated microglia recovered to the same density and similar transcriptional characteristics as those in control mice (19). The LORR and RORR of microglia-repopulated mice at D35 recovered to the same level as those of naïve mice at D0 (Figure 1B), indicating that fully repopulated microglia can reverse the anesthesia susceptibility of mice.

Together, our results indicate that microglial depletion by inhibiting CSF1R results in delayed anesthesia induction and early anesthesia emergence, making the animals more resistant to general anesthesia.

To further characterize the impact of microglial depletion throughout the anesthetization window, we recorded EEG and EMG signals to monitor the anesthesia state before and after pentobarbital administration (Figure 4A). Microglial depletion showed no obvious influence on the EEG in the awake or conscious state before pentobarbital administration (Figure 4B). In contrast, microglia-depleted mice exhibited delayed anesthesia induction and early emergence in response to pentobarbital (Figure 4B-C). In addition, microglial depletion significantly altered the power spectrum during anesthesia induction and emergence but not consciousness (Figure 4D). The EMG results showed that muscular activity in the conscious state was unchanged upon microglial depletion. In contrast, microglia-depleted mice exhibited a delayed loss and early recovery of muscular activity after pentobarbital injection (Figure 4E). Moreover, the probability of being in the conscious state, predicted by an algorithm combining EEG and EMG (34), triple confirmed delayed anesthesia induction and early emergence after microglial depletion (Figure 4F). Similar results were also observed for propofol (Figure 5) and ketamine (Figure 6). The EEG and EMG results demonstrate that microglial depletion impedes the anesthesia process.

Together, our results demonstrate that brain microglia-depleted mice are resistant to general anesthetics. In other words, microglia play important roles in facilitating and stabilizing the status of general anesthesia response.

Microglia facilitate the anesthesia response in a brain region-specific manner

A previous study indicated that microglia negatively regulate neuronal activity through the microglial catabolism of ATP and neuronal adenosine receptor A_1R. Microglial depletion enhances neuronal activity in the striatum (12). Different brain regions regulate anesthesia induction and emergence in diverse manners. If microglial depletion indiscriminately influences neuronal activities among different brain regions, the enhanced activities in AABRs and EABRs would be mutually antagonistic, complicating the anesthetic effect. To investigate whether microglia regulate neuronal

activity in an indiscriminate or brain region-specific manner, we examined c-Fos expression in AABRs and EABRs of CD- and PLX5622-treated mice (Figure 7A). We first studied AABRs, including the lateral habenula (LHb) (35, 36), supraoptic nucleus (SON) (37), ventrolateral preoptic nucleus (VLPO) (38) and thalamic reticular nucleus (TRN) (39). The abundance of c-Fos$^+$ cells was significantly reduced in the LHb and SON of microglia-depleted mice (Figure 7B). VLPO exhibited a decreasing trend in the abundance of c-Fos$^+$ cells, although it did not reach a statistically significant level ($P = 0.1592$) (Figure 7B). The abundance of c-Fos$^+$ cells was unchanged in the TRN (Figure 7B). We next examined EABRs, including the paraventricular thalamus (PVT) (40), locus coeruleus (LC) (41), lateral hypothalamus (LH) (42, 43) and ventral tegmental area (VTA) (44, 45). In contrast to a suppressed trend in AABRs, neuronal activity exhibited an enhanced trend in EABRs. Microglial depletion significantly increased the c-Fos$^+$ cell number in the PVT and LC (Figure 7C). c-Fos$^+$ cell numbers were also increased in the LH and VTA, although the difference did not reach statistical significance ($P = 0.0598$ and 0.1436, respectively) (Figure 7C). To exclude the possibility that the different c-Fos$^+$ cell numbers were attributed to animal handling, we compared c-Fos expression in saline-injected and noninjected mice (Figure 8A). Our results indicate that animal handling (saline injection) did not influence c-Fos expression in the LHb, SON, VLPO, TRN, PVT, LC, LH or VTA (Figure 8B-C). Therefore, we found that microglial depletion negatively regulates AABRs and positively regulates EABRs, indicating that microglia regulate neuronal activity in a brain region-specific manner. The suppressed neuronal activity in AABRs leads to delayed anesthesia induction. In contrast, the elevated neuronal activity in EABRs results in the early emergence of anesthesia.

The protein expression of c-Fos is relatively slow, peaking at a timepoint hours after transcription (46). Mice in our study were quickly sacrificed after deep anesthesia, typically within 5 to 10 min. The abundance of c-Fos protein seen with immunostaining reflected neuronal activity during the consciousness stage (Figure 7). In contrast, the mRNA expression of *Fos* (encoding c-Fos) is relatively fast, peaking at approximately

30 min after induction (46). We asked how microglia influence neuronal activity during the anesthesia stage and whether microglia differentially influence neuronal activity between the consciousness and anesthesia stages. To this end, we sacrificed microglia-naïve and microglia-depleted mice 30 min after deep anesthetization by pentobarbital and simultaneously labeled the c-Fos protein by immunostaining and *Fos* mRNA by RNAscope (Figure 9A). The c-Fos$^+$ cells represent activated neurons during the consciousness stage, while *Fos*$^+$ cells represent activated neurons during the anesthesia stage (Figure 9A). We compared the c-Fos$^+$ and *Fos*$^+$ cells in AABRs and EABRs in which neuronal activity was significantly altered in microglia-depleted mice, including the LHb, SON, PVT and LC (Figure 7B-C and Figure 9B-C). After microglial depletion, activated neurons in the anesthesia stage (*Fos*$^+$) displayed similar trends as those in the consciousness state (c-Fos$^+$) in the LHb, SON and LC (Figure 9B-C). However, the number of anesthesia-activated neurons (*Fos*$^+$) was unchanged between the naïve and microglia-depleted PVT, whereas the number of consciousness-activated neurons was significantly increased upon microglial depletion (Figure 9C). Exploiting the c-Fos protein and *Fos* mRNA dual labeling, we further compared consciousness-activated anesthesia-activated (c-Fos$^+$ *Fos*$^+$), consciousness-activated anesthesia-nonactivated (c-Fos$^+$ *Fos*$^-$) and consciousness-nonactivated anesthesia-activated (c-Fos$^-$ *Fos*$^+$) neurons between naïve and microglia-depleted mice (Figure 9A). In the LHb and SON of AABRs, consciousness-activated anesthesia-activated (c-Fos$^+$ *Fos*$^+$), consciousness-activated anesthesia-nonactivated (c-Fos$^+$ *Fos*$^-$) and consciousness-nonactivated anesthesia-activated (c-Fos$^-$ *Fos*$^+$) cell numbers exhibited a decreasing trend after microglial depletion (Figure 9B). This indicates that microglial depletion influences AABR neuronal activity at both the consciousness and anesthesia stages. In the PVT of the EABR, consciousness-activated anesthesia-nonactivated (c-Fos$^+$ *Fos*$^-$) cell numbers were significantly increased in microglia-depleted brains, whereas consciousness-activated anesthesia-activated (c-Fos$^+$ *Fos*$^+$) and consciousness-nonactivated anesthesia-activated (c-Fos$^-$ *Fos*$^+$) cell numbers were unchanged (Figure 9C). This indicates that microglial depletion influences PVT neuronal activity at the consciousness stage but not at the anesthesia stage. In the LC of the EABR, microglial

depletion significantly increased the cell numbers of consciousness-activated anesthesia-activated (c-Fos$^+$ *Fos*$^+$) and consciousness-activated anesthesia-nonactivated (c-Fos$^+$ *Fos*$^-$) neurons (Figure 9C). In contrast, the number of consciousness-nonactivated anesthesia-activated (c-Fos$^-$ *Fos*$^+$) cells was not altered (Figure 9C). This finding indicates that microglial depletion does not influence the LC neurons that are not activated in the consciousness stages.

The results indicate that microglia diversely regulate neuronal activity through a sophisticated brain region-specific manner instead of via indiscriminately negative feedback control as in the striatum (12). This may be due to microglial heterogeneity, different neuronal cell types, and/or circuitries in different brain regions.

Microglial depletion reduces the E/I ratio in AABR but enhances the E/I ratio in EABR

To understand how microglia reshape neuronal activity, we treated mice with CD or PLX5622 for 14 days and performed whole-cell recordings in neurons of SON and LC in acute brain slices, representing AABR and EABR with reduced and increased neuronal activity upon microglial depletion, respectively (Figure 10A). We delivered electrical pulses (0.1 ms in pulse duration, 10/20 Hz, 8 pulses) with a current intensity increment of 10 μA every 10 seconds to the neighboring tissue (approximately 50 μm from the recorded cell) to induce postsynaptic responses, including both evoked excitatory postsynaptic currents (eEPSCs) and evoked inhibitory postsynaptic currents (eIPSCs). In the SON of AABR, higher stimulation currents induced larger amplitudes of both eEPSCs and eIPSCs (Figure 10B-C). The peak amplitudes of eEPSCs in microglia-depleted mice were significantly smaller than those in naïve mice, while the peak amplitudes of eIPSCs showed no significant difference (Figure 10B-C). As shown in Figure 10C, the excitation received by SON neurons dominated in naïve mice. The E/I ratio was also significantly decreased after microglial depletion, indicating decreased neuronal excitability in the SON (Figure 10D). SON neurons with microglia depletion exhibited a significantly increased paired-pulse ratio (PPR) of eEPSCs, while

the eIPSC PPR was similar between naïve and microglia-depleted mice (Figure 10E-F), indicating a reduction in presynaptic release probability in excitatory synapses. Microglial depletion thus results in a more inhibitory state in the AABR SON. In the LC of EABR, the eEPSC amplitudes induced by higher stimulation currents in microglia-depleted mice were substantially greater than those in naïve mice (Figure 10G-H). In contrast, the eIPSC amplitudes showed no significant difference (Figure 10G-H). In contrast to that in the SON, the E/I ratio in the LC was significantly enhanced in PLX5622-treated mice (Figure 10I), indicating an increase in the excitation of LC neurons. Microglial depletion did not change the eEPSC PPR or eIPSC PPR in the LC (Figure 10J-K), representing an unchanged presynaptic release probability in both excitatory and inhibitory synapses. Microglial depletion thus results in a more excitatory state in the EABR LC.

In conclusion, our results reveal that microglial depletion decreases AABR and enhances EABR network activities, explaining delayed anesthesia induction and early emergence.

Microglia-mediated anesthesia modulation is not attributed to the influence of dendritic spines

Microglia play important roles in spine pruning (47, 48). We asked whether microglia-mediated anesthesia regulation occurs through the alteration of dendritic spines. We first quantified spine density after microglial depletion for 14 days (Figure 11A). Spine density in both apical and basal dendrites of layer V pyramidal cells in the medial prefrontal cortex (mPFC) was not changed in the relatively short period of 14 days (Figure 11B), when anesthesia induction and emergence were already robustly influenced (Figure 1). The ratios of spine categories of different shapes were altered in microglia-depleted mice. In apical dendrites, the percentage of mature mushroom spines was increased, whereas the percentage of filopodia spines was reduced (Figure 11B). In basal dendrites, mature mushroom spines were increased, while thin and filopodia spines were decreased (Figure 11B). Thus, short-term microglial depletion for

14 days does not alter spine density but changes the percentage of different categories of spines, even though general anesthesia is dramatically influenced. Next, we ask whether the altered spine density influences general anesthesia response. Microglia phagocytose dendritic spines via the C1q "eat me" signal (8, 47, 49). The dendritic spine is remodeled in C1q-dificient mice with increased density (50).We thus examined anesthesia induction and emergence in C1qa$^{-/-}$ mice (Figure 11C). Even with the alteration of spine density, the pentobarbital-, propofol- or ketamine-induced LORR and RORR were not influenced in C1q-deficient mice (Figure 11D). Therefore, our results reveal that even though microglia contribute to spine plasticity, microglia-mediated anesthesia modulation does not result from spine pruning.

Intracellular calcium in microglia regulates the anesthesia response through P2Y12 signaling

Microglial P2Y12 is a G protein-coupled receptor (GPCR) that modulates neuronal activity (11). We thus asked whether microglia-mediated anesthesia modulation is dependent on P2Y12. To address this question, we utilized the selective P2Y12 antagonist 2-MeSAMP (51) to block P2Y12 signaling by intracranial guide tube implantation (Figure 12A). Ninety minutes after 2-MeSAMP administration, brain microglia exhibited a more reactive morphology (Figure 12B), the consequence of decreased P2Y12 signaling, as shown in previous studies (52). Pharmacological inhibition of P2Y12 by 2-MeSAMP delayed the LORR and accelerated the RORR of pentobarbital-induced anesthetization (Figure 12C). To further confirm the function of microglial P2Y12 in the anesthesia response, we conditionally knocked out P2Y12 in microglia in CX3CR1$^{+/CreER}$::P2Y12$^{fl/fl}$ mice (Figure 12D). After 4 doses of tamoxifen, the majority of P2Y12 was successfully knocked out in CX3CR1$^{+/CreER}$::P2Y12$^{fl/fl}$ mice (Figure 12E). CX3CR1$^{+/CreER}$::P2Y12$^{fl/fl}$ mice exhibited delayed LORR and early RORR in response to pentobarbital (Figure 12F), echoing the pharmacological inhibition by 2-MeSAMP. Interestingly, when the conditional knockout of microglial P2Y12 was induced at a lower efficacy in TMEM119$^{CreER/CreER}$::P2Y12$^{fl/fl}$ mice (Figure 12G-H), as the recombinase activity of TMEM119-CreER is lower than that of

CX3CR1-CreER (53, 54), TMEM119$^{CreER/CreER}$::P2Y12$^{fl/fl}$ mice displayed an early RORR in response to pentobarbital, but the LORR was not affected (Figure 12I). The results indicate that microglia regulate the anesthesia response through P2Y12 signaling in a dose-dependent manner.

The influence of microglia replacement to the general anesthesia

In 2020, we first developed efficient strategies for microglia replacement and proposed therapeutic applications for neurological disorders (18). Microglia replacement by bone marrow transplantation (Mr BMT or mrBMT), one of the replacement strategies, can induce bone marrow cells (BMCs) to differentiate into microglia-like cells and efficiently replace endogenous microglia in the whole CNS (18, 55). Despite sharing similar characteristics to endogenous microglia, the replaced cells are P2Y12^{-} (Figure 13A-B) as we previously reported (18). We thus reasoned that if microglial P2Y12 indeed influences the response to general anesthesia, Mr BMT-treated mice with P2Y12^{-} microglia should display a dampened response to anesthetics. To this end, we examined anesthesia induction and emergence in Mr BMT mice (Figure 13A). We found that Mr BMT mice exhibited delayed LORR and early RORR (Figure 13C), further echoing the important regulatory role of P2Y12 in the response to general anesthesia.

Microglial intracellular calcium regulates general anesthesia

Purinergic activation of P2Y12 increases intracellular Ca^{2+} (23-25). We thus reasoned that the modulation of the anesthesia response is mediated by downstream Ca^{2+} signaling. To this end, we ectopically expressed a chemogenetic receptor in microglia by CX3CR1$^{+/CreER}$::hM3Dq-YFP$^{+/-}$ (Figure 14A-B). hM3Dq is a modified human M3 muscarinic (hM3) receptor that activates $G_{\alpha q}$ upon clozapine-N-oxide (CNO) and in turn enhances its downstream Ca^{2+} concentration (56, 57). When we treated CX3CR1$^{+/CreER}$::hM3Dq-YFP$^{+/-}$ with CNO to elevate the intracellular Ca^{2+} level in microglia, the LORR to pentobarbital was accelerated, and RORR was delayed (Figure 14C). On the other hand, STIM1 is an endoplasmic reticulum Ca^{2+} sensor. The lack of

382 STIM1 results in impaired store-operated Ca^{2+} influx (58-60). To specifically disrupt
383 intracellular Ca^{2+} signaling in microglia, we conditionally knocked out STIM1 in
384 microglia in CX3CR1$^{+/CreER}$::STIM1$^{fl/fl}$ mice. After tamoxifen induction, *Stim1* mRNA
385 was significantly reduced in the CX3CR1$^{+/CreER}$::STIM1$^{fl/fl}$ mouse brain (Figure 14D-
386 E). We found that with impaired Ca^{2+} signaling in microglia, CX3CR1$^{+/CreER}$::STIM1$^{fl/fl}$
387 mice displayed delayed anesthesia induction and early emergence (Figure 14F). By
388 both enhancing and disrupting microglial Ca^{2+}, our results reveal that intracellular Ca^{2+}
389 in microglia facilitates the anesthesia process.
390
391 Purinergic activation of P2Y12 enhances intracellular Ca^{2+} (23-25). Our results thus
392 indicate that microglia regulate the anesthesia process through P2Y12 and its
393 downstream Ca^{2+} signaling.
394
395

Discussion

The mutual interaction between microglia and neurons

Previous studies have indicated that microglia exhibit increased process motility, extension and territory surveillance during anesthetization and sleep (4, 5). However, whether and how microglia regulate neuronal activity and contribute to anesthesia response is largely unknown. Our study demonstrated an active role of microglia in neuronal activity that facilitate and stabilize the anesthesia response by differentially changing neuronal activity in the AABRs and EABRs. It relies on microglial P2Y12 and intracellular calcium, rather than the spines plasticity. Microglia and neurons mutually interact with each other under both physiological and pathological conditions. Previous studies have indicated that neurons can influence the morphology and function of microglia through neurotransmitters and/or neuromodulators, such as GABA and ATP (61, 62). On the other hand, microglia can regulate neuronal activity. Microglia in the paraventricular nucleus are able to maintain the balance of sympathetic outflow and suppress the pressor response under hypertensive insults (63). Chemogenetic manipulations of microglia lead to a prostaglandin-dependent reduction in the excitability of striatal neurons (64). This evidence reveals that although microglia are resident immune cells in the brain, their functions are not limited to the immune response. Our study found that during the process of general anesthesia, microglia serve as an “anesthesia facilitator and stabilizer” through activating AABRs and inhibiting EABRs. As a result, microglia-depleted mice are more resistant to general anesthesia.

Microglial depletion diversely influences neuronal activities in different brain regions

Different nuclei are involved in the response to general anesthesia. The influences of microglial depletion on neuronal activity among these nuclei are different. After microglial ablation, c-Fos expression is decreased in AABRs but increased in EABRs. Meanwhile, the electrophysiology results also show that the E/I ratio is differentially regulated in different brain regions upon microglial depletion. However, the mechanism

behind brain region-specific regulation is unclear. Several hypotheses may explain the microglia-mediated diverse regulations among different brain regions. First, it may be due to microglial heterogeneity among brain regions. Nonetheless, recent study indicated that the cross-regional heterogeneity in adulthood was over estimated in previous studies (65). Second, different neuronal cell types may differentially respond to microglial depletion. Taking the adenosine receptor as an example. The adenosine concentration is reduced in the microglia-depleted cortex (66). Interference of P2Y12, CD39 or CD73 in microglia disrupts the metabolism of extracellular adenosine in the brain (67). Our results showed that inhibition or knockout of P2Y12 results in resistance of general anesthesia, indicating that neurons in different brain regions, e.g., the AABRs and EABRs, differentially respond to adenosine. Moreover, adenosine receptor subtypes are discriminately distributed across different brain regions (68), suggesting neurons of different adenosine receptors in the different brain regions may differentially respond to adenosine. Third, the brain region-specific regulation may also rely on the neural circuitry. Mutual innervations of the AABRs-EABRs and local circuities within specific brain region can result in the diverse neuronal response. The regulation of neuronal activity is an overall effect that integrated with multiple variables. So does the microglial contribution to the different brain regions.

Molecular mechanisms of how microglia regulate neuronal activity

The C1q-dependent spine pruning by microglia mediates memory forgetting (69). With increased number of dendritic spines, C1q-deficient mice display enhanced synaptic connectivity and seizure susceptibility (70). These indicate the importance of C1q in maintaining the neural function. However, we did not observe the alteration of general anesthesia response. Moreover, the spine density was not changed upon the short-term microglial depletion for 14 days. Consequently, our results indicate the microglia-mediated regulation of anesthesia response does not result from dendritic spine. In striatum, microglia serve as a brake suppressing neuronal activity (12). P2Y12 knockout in microglia augments the epilepsy susceptible (71, 72). These evidences indicate that P2Y12 signaling is critical to the stability of neuronal network. However,

when we compared neuronal activities by c-Fos staining and patch clamp recording between the AABRs and EABRs, we observed different consequences to the microglial depletion. With suppressed neuronal activity in AABRs and enhanced neuronal activity in EABRs, microglial depletion results in delayed anesthesia induction and early emergence. Our results also indicate that microglia sophisticatedly and diversely contribute to orchestrating the CNS function, rather than play an indiscriminate role of negative feedback control as they do in the striatum (12). Notably, P2Y12 is down regulated in several neurological disorders (73). The consequences of P2Y12 downregulation in neurological disorders are largely unknown. It would be a potential therapeutic target to harness neurological disorders.

Microglia replacement and general anesthesia

In 2020, we first developed three strategies to achieve efficient microglia replacement (18), including Mr BMT (18, 55), microglia replacement by peripheral blood (Mr PB or mrPB) (18, 74) and microglia replacement by microglia transplantation (Mr MT or mrMT) (18, 75). We discussed a potential application for treating Alzheimer's disease (AD) by replacing microglia deficient in TREM2, which is one of the major risk factors in sporadic AD (76-84), with TREM2-normal microglia (18, 85, 86). Recent studies verified this therapeutic effect of Mr BMT in an AD mouse model (87, 88), demonstrating the clinical potential of microglia replacement. It also provides new and clinically feasible strategies for treating other neurological disorders (18, 85, 86, 89). Despite sharing similar characteristics with naïve microglia, Mr BMT cells are P2Y12^{-} (18). Whether P2Y12^{-} microglia-like Mr BMT cells influence the response to general anesthesia is unknown. To this end, we tested the response to general anesthesia use in mice treated with Mr BMT and found delayed anesthesia induction and early emergence. This study not only demonstrates the role of P2Y12 signaling in regulating the response to general anesthesia but also identifies an impeded general anesthesia response after Mr BMT treatment.

Optogenetic and chemogenetic manipulations in neuronal and nonneuronal cells

The "activation" and "inhibition" of neurons are defined as the electrical activities (e.g., action potentials) by which neurons convey information and signals. Optogenetics and chemogenetics are powerful tools widely used in manipulating neuronal electrical activity to dissect neural circuitries. Optogenetics relies on light-sensitive ion channels, pumps or enzymes. Channelrhodopsin-2 (ChR2) is an excitatory optogenetic tool of light-sensitive cation channels from green algae (90). Ectopically expressed ChR2 in neurons responds to blue light and undergoes a conformational change, which allows the passive diffusion of Na^+, Ca^{2+}, H^+ and K^+. It thus depolarizes the member potential and elicits action potentials in neurons (91, 92). Halorhodopsin (NpHR) is an inhibitory optogenetic tool of archaeal light-driven chloride pumps. In response to yellow light, the ectopically expressed NpHR in neurons actively pumps Cl^- into cells and hyperpolarizes the membrane potential (93). Chemogenetic tools are based on designer receptors exclusively activated by designer drugs (DREAADs) (56). hM3Dq is an excitatory chemogenetic tool of genetically encoded tetracycline-sensitive G protein-coupled receptor (GPCR) (94). hM3Dq responds to CNO and activates intracellular $G_{\alpha q}$. Then, the elevated $G_{\alpha q}$ level enhances the intracellular Ca^{2+} concentration, thereby inducing action potentials in neurons. hM4Di is an inhibitory chemogenetic tool (95). hM4Di responds to CNO and engages the $G_{\alpha i}$ signaling pathway. $G_{\alpha i}$ in neurons reduces intracellular Ca^{2+} (suppressing presynaptic transmitter release) and opens K^+ channels (hyperpolarizing the membrane potential). Thus, the intracellular consequences from optogenetic and chemogenetic manipulations can drive or suppress action potentials in neurons, thus "activating" or "inhibiting" the neuron.

In contrast, the nonelectrically excitable cells, including microglia, have no action potentials. The "activation" (or reactive state) and "inhibition" are not defined as electrical activities. Instead, "activation" (or reactive state) and "inhibition" are defined as responses to specific stimuli in diverse contexts in which nonneuronal cells experience sophisticated alterations. The intracellular events of optogenetic and chemogenetic tools are not directly associated with nonneuronal cell activation. Thus, optogenetic and chemogenetic tools do not simply "activate" or "inhibit" nonneuronal

cells in the brain. In our study, we ectopically expressed hM3Dq in microglia. Upon CNO administration, hM3Dq elevates intracellular Ca^{2+} levels. It does not result in action potentials in microglia and thus does not "activate" microglia. Nonetheless, it is a reliable chemogenetic tool for manipulating the Ca^{2+} level in microglia. We used this approach to investigate the biological function of microglial Ca^{2+} in the response to general anesthesia. Together, optogenetic and chemogenetic tools do not simply "activate" or "inhibit" nonneuronal cells. Instead, they can be utilized to study the function of nonneuronal cells regarding specific intracellular events.

Methods

Animals

C57BL/6J mice were purchased from SPF (Beijing) Vital River Laboratory Animal Technology. P2Y12$^{fl/fl}$ mice (72) were donated by Prof. Jiyun Peng at Nanchang University. TMEM119-CreER mice (C57BL/6-Tmem119$^{em1(cre/ERT2)Gfng}$/J, Stock #: 031820) (96), CX3CR1-CreER mice (B6.129P2(C)-Cx3cr1$^{tm2.1(cre/ERT2)Jung}$/J, Stock#: 020940) (97), C1qa$^{-/-}$ mice (B6(Cg)-C1qa$^{tm1d(EUCOMM)Wtsi}$/TennJ, Stock#: 31675) (98), β-actin-GFP mice (C57BL/6-Tg (CAG-EGFP) 131Osb/LeySopJ, Stock#: 006567) (99) and LSL-hM3Dq-YFP mice (B6N;129-Tg(CAG-CHRM3*, -mCitrine)1Ute/J, Stock#: 026220) (100) were purchased from Jackson Lab. STIM1$^{fl/fl}$ mice (C57BL/6JGpt-Stim1^{em1Cflox}/Gpt, Stock#: T013158) were purchased from GemPharmatech. All mice were housed in the Animal Facility at the Department of Laboratory Animal Science at Fudan University under a 12-hour light/dark cycle with food and water given *ad libitum*. All animal experiments were conducted in accordance with the guidelines of the Institutional Animal Care and Use Committee of the Department of Laboratory Animal Science at Fudan University.

Chemicals and reagents

PLX5622 was formulated into the AIN-76A diet at a concentration of 1.2 g of PLX5622 per kilogram of diet by SYSE Bio (Cat#: D20010801). PLX73086 (Plexxikon) was formulated into the AIN-76A diet at 0.2 g of PLX73086 per kilogram of diet by Research Diet, Inc. (Cat#: D15180708i). The normal AIN-76A diet (control diet, CD) was purchased from SYSE Bio (Cat#: PD1001). Chloral hydrate (Cat#: C104202) and tamoxifen (Cat#: T137974) were purchased from Aladdin. The P2Y12 inhibitor 2-MeSAMP (Cat#: HY-125989) and the DREADD agonist CNO (Cat#: HY-17366) were purchased from MCE. Xylazine hydrochloride (Cat#: X1251) were purchased from Sigma-Aldrich. Propofol (H20123318) was purchased from Xi'an Libang Pharmaceutical. Ketamine (H20193336) was purchased from Shanghai Pharmaceutical. Isoflurane (Lot#: 20230501) was purchased from RWD.

554

555 **Drug administration**

556 To pharmacologically ablate myeloid cells, mice were administered a PLX5622-
557 formulated AIN-76A diet (1.2 g PLX5622 per kilogram of diet, formulated by SYSE
558 Bio) *ad libitum* for 14 days. To pharmacologically ablate peripheral macrophages, mice
559 were administered a PLX73086-formulated AIN-76A diet (0.2 g PLX73086 per
560 kilogram of diet, formulated by Research Diet) *ad libitum* for 14 days. Control mice
561 were fed an AIN-76A control diet (CD). Since the microglial ablation efficiency by
562 CSF1R inhibition might be different between sexes (101), we utilized male mice for
563 this experiment. To efficiently induce CreER-dependent recombination, tamoxifen (150
564 mg per kg of body weight) dissolved in olive oil (Macklin, 0815210) was administered
565 via oral gavage for 4 consecutive days following our previously described procedures
566 (15-19). 2-MeSAMP (10 mM) was injected into the lateral ventricle 90 min before the
567 behavior test (52). CNO (100 μg/mL) was administered via intraperitoneal injection 90
568 min before the behavior test (102).

569

570 **Righting reflex**

571 First, the mice were placed in a box for 5 min for adaptation to the experimental
572 environment. Next, anesthesia was initiated, and the righting reflex of the mice was
573 checked every 15 s from the beginning of anesthesia. When the mice were in an
574 abnormal position (limbs up) and could not voluntarily return to the normal position,
575 this behavior was defined as the LORR. The mouse was kept in a position with its back
576 touching the ground and limbs facing upward during deep anesthesia. A thermostatic
577 heating pad (37 °C) was placed under the body to maintain body temperature. If the
578 mouse automatically returned to the normal position (all limbs touching the ground)
579 from the position where the righting reflex disappeared, it was considered to have
580 recovered. The time from the end of anesthesia to RORR was defined as the time of
581 emergence from anesthesia. All experiments were conducted between 20:00 and 4:00
582 the next day, in the same light-dark cycle of ZT 12:00 to 20:00.

583

584 **Brain tissue preparation**

585 Mice were deeply anesthetized with a mixture of ketamine hydrochloride (100 mg per
586 kg of body weight) and xylazine (10 mg per kg of body weight) by intraperitoneal
587 injection. For histological experiments, animals were sequentially transcranially
588 perfused with 0.01 M PBS and 4% paraformaldehyde (PFA) (Biosharp, Cat#: BL539A)
589 in 0.01 M PBS. Brains were then carefully harvested and postfixed in 4% PFA in 0.01
590 MPBS at 4 °C overnight.

591

592 **Cryosection preparation**

593 Brains and peripheral organs were dehydrated in 30% sucrose in 0.01 M PBS at 4 °C
594 for 3 days. After being embedded in optimal cutting temperature compound (OCT,
595 SAKURA, Cat#: 4583), brain and peripheral organ samples were frozen and stored at
596 -80 °C before sectioning. Tissue with regions of interest was cut by a cryostat (Leica,
597 CM1950) at a thickness of 35 μm.

598

599 **Immunohistochemistry and image acquisition**

600 Brain and peripheral organ sections were rinsed with 0.01 M PBS 3 times for 10 to 15
601 min, followed by blocking with 4% normal donkey serum (NDS, Jackson, Cat#: 017-
602 000-121) in 0.01 M PBS containing 0.3% Triton X-100 (Aladdin, Cat#: T109026)
603 (PBST) at room temperature (RT) for 2 hours. Then, the samples were incubated with
604 primary antibodies with 1% NDS in PBST at 4 °C overnight. After rinsing with PBST
605 for 3 changes, the samples were incubated with fluorescent dye-conjugated secondary
606 antibodies with 1% NDS in PBST with 4',6-diamidino-2-phenylindole (DAPI, 1:1000,
607 Sigma-Aldrich, D9542) at RT for 2 hours. Afterward, the samples were rinsed three
608 times before mounting with anti-fade mounting medium (SouthernBiotech, Cat#: 0100-
609 01).

610

611 Primary antibodies included rabbit anti-IBA1 (1:500, Wako, Cat#: 019-19741, Lot:
612 CAJ3125), goat anti-IBA1 (1:500, Abcam, Cat#: ab5076, Lot: GR3425808-1), rabbit
613 anti-GFP (1:1000, Invitrogen, Cat#: A11122, Lot: 2273763), rabbit anti-c-Fos (1:1000,

Abcam, Cat#: ab190289, Lot: GR3367372-1), and rabbit anti-P2Y12 (1:500, Sigma-Aldrich, Cat#: S5768, Lot: 0000128079). Secondary antibodies included AF488 donkey anti-rabbit (1:1000, Jackson, Cat#: 711-545-152, Lot: 161527), AF568 donkey anti-rabbit (1:1000, Invitrogen, A10042, Lot: 2433862), AF568 donkey anti-goat (1:1000, Invitrogen, Cat#: A11057, Lot: 2160061), and AF647 donkey anti-goat (1:1000, Jackson, Cat#: 705-605-003, Lot: 147708).

Confocal images were acquired by using an Olympus FV3000 confocal microscope with a solid-state laser. Lasers with wavelengths of 405 nm, 488 nm, 561 nm and 640 nm were used to excite the fluorophores. 60X (oil), 40X (oil) and 20X objectives were utilized. Some whole brain fluorescence images were acquired by an Olympus VS120 microscope equipped with a motorized stage. 10X objective was used. Z stacked focal planes were acquired and maximally projected with Fiji. The brightness and contrast of the image were adjusted with Fiji if necessary.

c-Fos immunostaining and *Fos* RNAscope dual labeling

Mice were fed a CD or PLX5622 for 14 days and placed alone in a quiet environment for 2 h, and samples were taken 30 min after intraperitoneal injection of pentobarbital sodium (80 mg/kg BW). Cryostat sections at 15 μm were collected, and hybridizations were carried out according to the manufacturer's instructions using RNAscope Multiplex Fluorescent Detection Reagents V2 (Advanced Cell Diagnostics, Cat#: 323110, Lot: 2015636, 2019446). Briefly, sections were dehydrated in sequential incubations with ethanol, followed by 30 min Protease Plus treatment and RNAscope wash buffer wash. Mouse *Fos* probe (Cat#: 316921, Lot: 221048) was incubated for 2 h at 40 °C, followed by three amplification steps. After all these steps, general immunostaining steps were performed as aforementioned.

EEG/EMG surgery and recording

The mice were initially anesthetized by 2% isoflurane and maintained under anesthesia by 1% isoflurane during the surgery. Body temperature was monitored in real time and

kept at approximately 37 °C throughout the surgical procedure. For the EEG/EMG recording experiment, two stainless steel screws were placed on the prefrontal cortex (recording site) and cerebellar cortex (reference site) as EEG electrodes, and two other thin stainless-steel wires were inserted into the bilateral neck muscles as EMG electrodes.

Mice were allowed a minimum of 7 days of recovery following surgery. On the day of recording, the mice were acclimated first for 20 min in a recording box, where the temperature was kept at 25 °C, and the mice were allowed to move around freely. All recordings were conducted between 20:00 and 24:00 Signals were amplified (Apollo I, Bio-Signal Technologies, USA) and digitized at a sampling rate of 1000 Hz.

EEG spectra analysis

The raw EEG signals were down sampled to 250 Hz before analysis. The power spectrum was computed using multitaper methods in the MATLAB Chronux toolbox (version 2.1.2, http://chronux.org/), with 4 s data segments and 3-5 tapers (TW = 3, K = 5). To normalize total power and to compare between groups, the power spectra were normalized such that the total area under the spectra was unity (e.g., power spectral density). Power spectral density analysis was performed on the data from the baseline (20 min before injection), induction (slow oscillation appears for the first time and lasts for more than 30 s after injection) and emergence (slow oscillation disappears for the first time and lasts for more than 10 min after deep anesthesia) periods.

The time-frequency power spectrum (by the “cwt” function in the MATLAB wavelet toolbox) was also computed using 80 Hz down sampled EEG to enhance the temporal resolution.

Root mean square of EMG

The raw EMGs were further down sampled to 25 Hz. The root mean square (RMS) was obtained using a 20 s moving window.

Consciousness probability

The vigilance states before and after injection of anesthetic were automatically classified as *awake* and *nonawake* states by using artificial intelligence (AI)-driven software Lunion Stage (https://www.luniondata.com, Shanghai, China) and were checked manually (34). The awake probability was generated by 1,000 repeat bootstrap analyses, e.g., for each repeat, we randomly selected 75% of the total animal data to calculate the percentage of animals in the awake state at each time point. Any epochs considered to contain significant movement artifacts were omitted from the data analysis.

Intracranial guide tube implantation and microinjection

Briefly, mice were anesthetized with 3% isoflurane (RWD, Lot: 20230501) delivered in 100% O_2 and then transferred to a stereotaxic frame with a mouse anesthesia mask (RWD, China). The delivered isoflurane concentration was decreased to 1.5%. A thermostatic heating pad (37 °C) was placed under the mouse to maintain body temperature. Unilateral lateral ventricle cannulas were implanted in targeted coordinates (anteroposterior: -0.5 mm; mediolateral: 1 mm; dorsoventral: -2.3 mm) in 8-week-old mice (103, 104). After a 7-day recovery from surgery, 5 μL of 2-MeSAMP (10 mM) was injected via the guide cannula using a microsyringe pump at a rate of 0.5 μL/min according to the manufacturer's instructions. Behavioral tests were performed 90 min after the intraventricular injection.

Microglia replacement by bone marrow transplantation (Mr BMT)

Two approaches were used to achieve myeloid ablation/inhibition of Mr BMT in this study. For Mr BMT by irradiation, 8-week-old recipient mice were fed PLX5622 from day 0 to day 14. Then, the pretreated mice were exposed to 9 Gy X-ray irradiation on day 14 (18, 55). For Mr BMT by busulfan, 8-week-old recipient mice were fed PLX5622 from day 0 to day 14. Then, the mice received busulfan (25 mg/kg of body weight for each day) from day 9 to day 12 by intraperitoneal injection. Afterward, 1×10^7 bone marrow cells harvested from the tibia and femur of the β-actin-GFP donor mouse were immediately introduced into the recipient mice on day 14 via intravenous

injection. Then, the mice were fed a control diet. The mouse was fed neomycin (1.1 g/L) in acidic water (pH 2-3) throughout the procedure of microglia replacement.

Acute brain slice preparation for patch clamp recording and spine quantification

Parasagittal slices containing the LC, SON and mPFC were obtained from mice aged from postnatal day 60 (P60) to P70. Mice were deeply anesthetized with pentobarbital sodium (80 mg/kg of body weight) before sacrifice by decapitation. The brain was quickly removed and immersed in ice-cold sucrose-based ACSF (10 mM glucose, 213 mM sucrose, 26 mM $NaHCO_3$, 1.25 mM NaH_2PO_4, 2.5 mM KCl, 2 mM $MgSO_4$, 2 mM $CaCl_2$). Acute brain slices with a thickness of 300 μm were cut in sucrose-based ACSF by a vibratome (Leica VT 1200S). Afterward, brain slices were immediately transferred to an incubation chamber filled with 95% O_2 and 5% CO_2 equilibrated normal ACSF (25 mM glucose, 126 mM NaCl, 26 mM $NaHCO_3$, 1.25 mM NaH_2PO_4, 2.5 mM KCl, 2 mM $MgSO_4$ and 2 mM $CaCl_2$) at 34 °C for 45 min. Slices were then transferred to 95% O_2 and 5% CO_2 equilibrated normal ACSF at room temperature before recording. Slices were then transferred to a recording chamber continuously perfused in 95% O_2 and 5% CO_2 equilibrated normal ACSF (approximately 60 mL/h) with the temperature maintained at 34 ± 1 °C. An infrared-differential interference contrast (IR-DIC) microscope (Olympus BX-51WI) was used for visualization of individual neurons.

Patch clamp recording

The intracellular solutions contained 138 mM $CsCH_3SO_3$, 3 mM CsCl, 2 mM $MgCl_2$, 0.2 mM EGTA, 10 mM HEPES, 2 mM ATP-Na_2 and 5 mM QX314. The pH was appropriately adjusted to 7.3 by CsOH, and osmolarity was adjusted to 280-290 mOsm. The electrode impedance was approximately 4 to 7 MΩ. When recording the evoked EPSCs (eEPSCs), the membrane potential was held at -70 mV. After eEPSC recording, the same cell was held at 0 mV to record evoked IPSCs (eIPSCs). The locations of SON and LC were identified under an IR-DIC microscope based on their location and cell density. The stimulating electrode was placed deep inside the nucleus and approximately 50 μm from the recorded cell. Membrane voltage and current were

sampled at 10-25 kHz and low-pass filtered at 2-10 kHz using the patch clamp amplifier MultiClamp 700B (Molecular Devices, LLC), digitized and sampled by Micro 1401 with Spike2 software (Cambridge Electronic Design) or by Digidata 1440A with pCLAMP 10.2 software (Molecular Devices, LLC). The evoked postsynaptic currents were analyzed by MATLAB R2023a (MathWorks) and OriginPro9.1 (Originlab, Inc.).

Biocytin filling and morphological reconstruction

Coronal sections containing the mPFC, SON and LC were recorded using patch clamp under a whole-cell configuration. The electrode was filled with the patch solution with 0.2% biocytin (Life Technologies, B1592). Neurons that maintained a stable membrane potential for at least 20 min were included. Upon cessation of filling, the pipette was slowly pulled out along the direction of recording until a membrane reseal was formed. After a 10 min recovery, the slices were fixed in 4% paraformaldehyde overnight at 4 °C, cryoprotected in 30% sucrose solution (for 1 to 3 days) and incubated with AF488 streptavidin (1:1000, Invitrogen, Cat#: S11223, 2390711) in PBS containing 0.3% Triton X-100 (Aladdin, T109026) overnight at 4 °C. To reconstruct the dendritic spines, the coronal sections were resected at 70 μm thickness and coverslipped with the mounting medium Fluoromount-G (Southern Biotechnology Associates). The images were taken using an Olympus FV3000 confocal microscope equipped with a UPLSAPO 60X oil-immersion lens (numerical aperture of 1.5). The 2048 × 2048 pixels frame size was used without zooming. Serial Z-stack images with a step size of 0.7 μm were collected. Dendritic segments located 30 μm away from the soma and 50 μm in length were selected for analysis of spine density and category. For individual cells, 8 to 12 dendritic segments were chosen for analysis. Dendritic length and spines were counted and categorized with ImageJ (NIH). Spines were classified into three subtypes: thin, mushroom, and stubby based on previously described criteria (105). Briefly, thin spines included a head-to-neck diameter ratio less than 1.1 and a length-to-spine head ratio greater than 2.0. Mushroom spines had a head diameter larger than 0.5 mm and a head-to-neck diameter ratio greater than 1.1. Stubby spines had no clear border between

763 the head and the attachment to the shaft. Filopodia had a long thin protrusion but
764 without a clear head shape.
765
766 **RNA extraction and qPCR**
767 Total RNA from brain tissue was extracted with TRIzol. cDNA was reverse transcribed
768 from total RNA using the Vazyme HIScript III RT SuperMix for qPCR kit according to
769 the manufacturer's instructions. Subsequently, a 20 μL reaction system was prepared
770 for qPCR using Vazyme ChamQ Universal SYBR qPCR Master Mix kit with an ABI
771 StepOne Plus Real-Time PCR system. The relative cDNA concentrations of target
772 genes were normalized to Gapdh. The primers used in this study were synthesized by
773 Tsingke Biotechnology, including:
774 *Gapdh*-forward (TGAGGCCGGTGCTGAGTATG),
775 *Gapdh*-reverse (TGGTTCACACCCATCACAAACA),
776 *Stim1*-forward (CAGGTTCAGTGAGACCCTGTC),
777 *Stim1*-reverse (GCCCACCAAGATCTCCACAA).
778
779 **Statistics and reproducibility**
780 The statistical approaches are indicated in the figure legends. For the righting reflex
781 test, block randomization was performed on cages of mice such that an approximate
782 number of mice per cage were assigned to each experimental group. Collection of
783 behavior experiment data was double blinded. c-Fos$^+$/*Fos*$^+$ cell counting and spine
784 morphology analysis were evaluated independently by two blinded experienced
785 researchers by Fiji. No statistical methods were used to predetermine sample sizes, but
786 our sample sizes were similar to those reported in our previous publications (15-19,
787 106). The data distribution was assumed to be normal, but this assumption was not
788 formally tested. No data were excluded from the analyses. Data are shown as the mean
789 ± SD or mean ± SEM as specifically identified. The two-tailed unpaired t test, paired t
790 test and one-way or two-way repeated measures (RM) ANOVA followed by
791 Bonferroni's multiple comparisons test were used to assess statistical significance based
792 on GraphPad Prism 9.0 and MATLAB 2020b if necessary. Significance was defined as

793 $P < 0.05$. The layout of all of the figures was generated by Adobe Illustrator.

794

795

Acknowledgements

The authors thank Lize Xiong (Shanghai Fourth People's Hospital, School of Medicine, Tongji University), Weifeng Yu (Renji Hospital, Shanghai Jiao Tong University), Zhian Hu (Army Medical University), Ji Hu (ShanghaiTech University), Zhe Zhang and Huateng Cao (Institute of Neuroscience, Chinese Academy of Sciences) and for the advice in this study, Jiyun Peng (Nanchang University) for donating the $P2Y12^{fl/fl}$ mice. This study was supported by STI2030-Major Projects (2022ZD0204700) (B.P.), (2022ZD0207200) (Y.R.) and (2021ZD0202500) (Y.S.), National Natural Science Foundation of China (32170958) (B.P.), (32000678) (Y.R.), (32130044, T2241002) (Y.S.), (32100930) (Q.H.) and (32200953)(W.K.), “Shuguang Program” supported by Shanghai Education Development Foundation and Shanghai Municipal Education Commission (22SG07) (B.P.), Program of Shanghai Academic/Technology Research Leader (21XD1420400) (B.P.), Shanghai Pilot Program for Basic Research (21TQ014) (B.P.), The Innovative Research Team of High-Level Local University in Shanghai (B.P.), Shanghai Municipal Science and Technology Major Project (2018SHZDZX01) (Y.M.), and ZJ Lab (Y.M.).

Author contributions

B.P. accidentally observed an anesthetic-resistant phenotype in microglia-depleted mice in 2015. B.P., Y.H. and Y.S. conceived and designed this study. B.P. and Y.S. supervised and conceptualized this study. Y.H. performed most of the experiments and data analysis unless specified. Y.H. and Q.H. conducted EEG and EMG experiments. T.L., W.K. and S.D. conducted patch clamp recordings. T.L. and Y.H. performed the spine analysis. X.L. performed RNAscope. B.P., Y.S., Y.R., Y.M., F.G., and W.L. provided necessary study support. All authors discussed the results and commented on this manuscript.

Competing interests

The authors declare no competing interests.

Figures

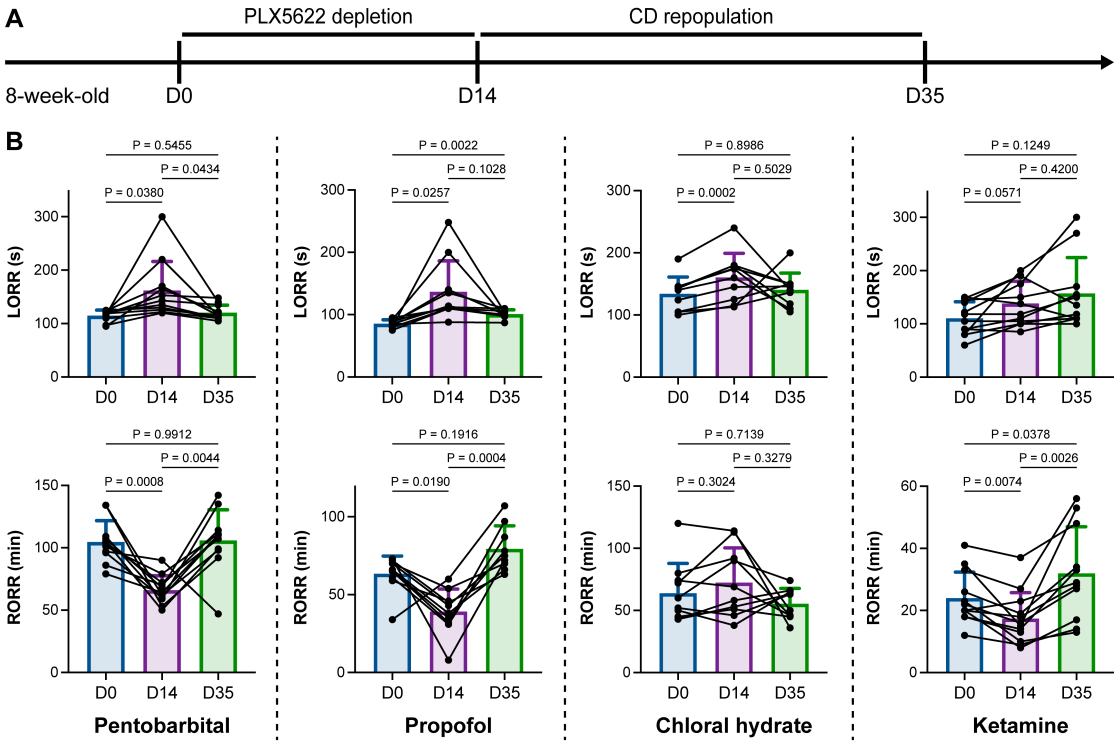

Figure 1 Microglial depletion impedes anesthesia induction and accelerates emergence. **(A)** Scheme of time points for microglial depletion and repopulation by PLX5622 and CD.

(B) Mice exhibit delayed induction and early emergence in pentobarbital-, propofol-, chloral hydrate- and ketamine-induced anesthesia. N = 11, 10, 10 and 12 mice for pentobarbital, propofol, chloral hydrate and ketamine, respectively. Repeated measures (paired) one-way ANOVA with Geisser-Greenhouse correction and Tukey's multiple comparison test.

Data are presented as mean ± SD. PLX5622: PLX5622-formulated diet; CD: control diet; LORR: loss of righting reflex; RORR: recovery of righting reflex.

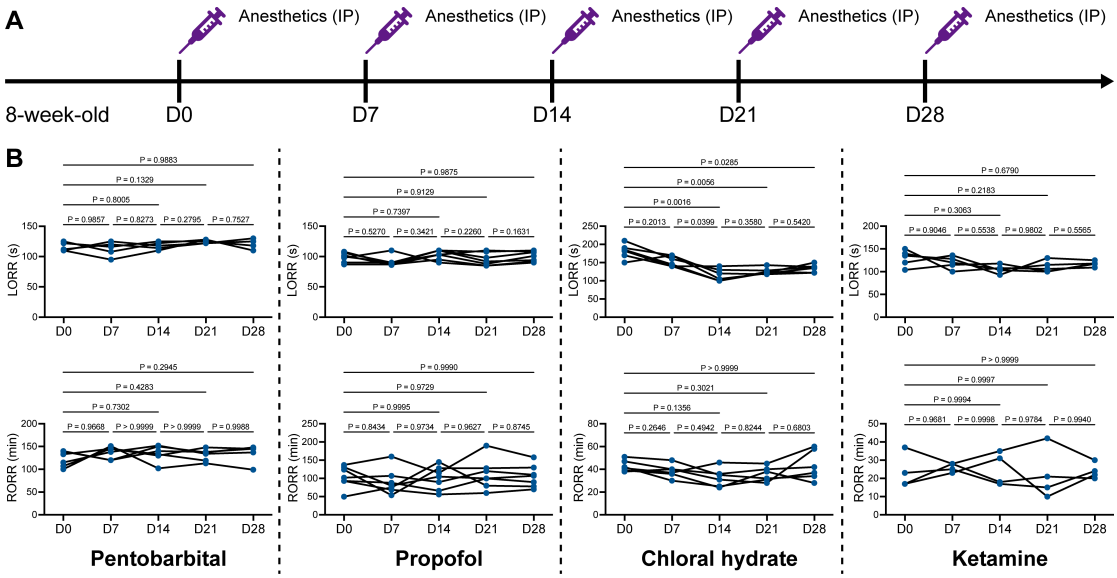

Figure 2 Repetitive anesthetic treatment does not result in anesthesia tolerance. **(A)** Scheme of time points for anesthetic treatments and righting reflex examination. **(B)** Repetitive treatment with pentobarbital, propofol, chloral hydrate or ketamine does not induce anesthesia tolerance in mice. N = 5, 7, 6 and 5 mice are treated with pentobarbital, propofol, chloral hydrate and ketamine, respectively. Repeated measures (paired) one-way ANOVA with Geisser-Greenhouse correction and Tukey's multiple comparison test. LORR: loss of righting reflex; RORR: recovery of righting reflex.

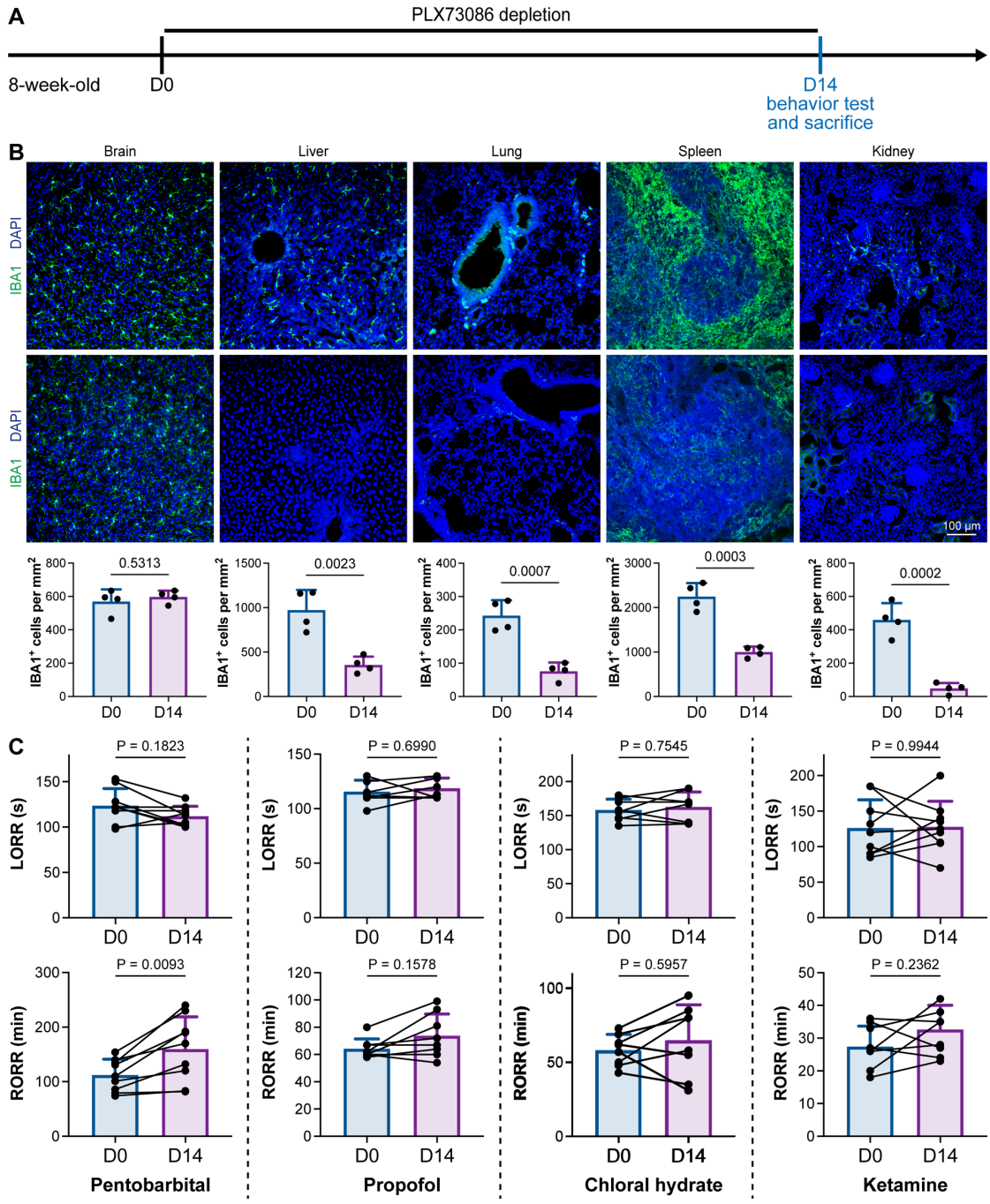

Figure 3 CSF1R inhibition-induced general anesthesia regulation is not due to the depletion of peripheral macrophages.

(A) Scheme of time points for peripheral macrophage depletion by PLX73086.

(B) CSF1R inhibition by PLX73086 dramatically ablates macrophages in the liver, lung, spleen and kidney and does not ablate brain microglia. N = 4 mice for each group. Two-tailed independent t test.

(C) Depletion of peripheral macrophages does not influence the anesthesia induction of pentobarbital, propofol, chloral hydrate and ketamine or the emergence from

propofol, chloral hydrate and ketamine. However, it impedes anesthesia emergence from pentobarbital. N = 9, 8, 8 and 9 mice for pentobarbital, propofol, chloral hydrate and ketamine, respectively. Two-tailed paired t test.

Data are presented as mean ± SD. PLX73086: PLX73086-formulated diet; CD: control diet; LORR: loss of righting reflex; RORR: recovery of righting reflex.

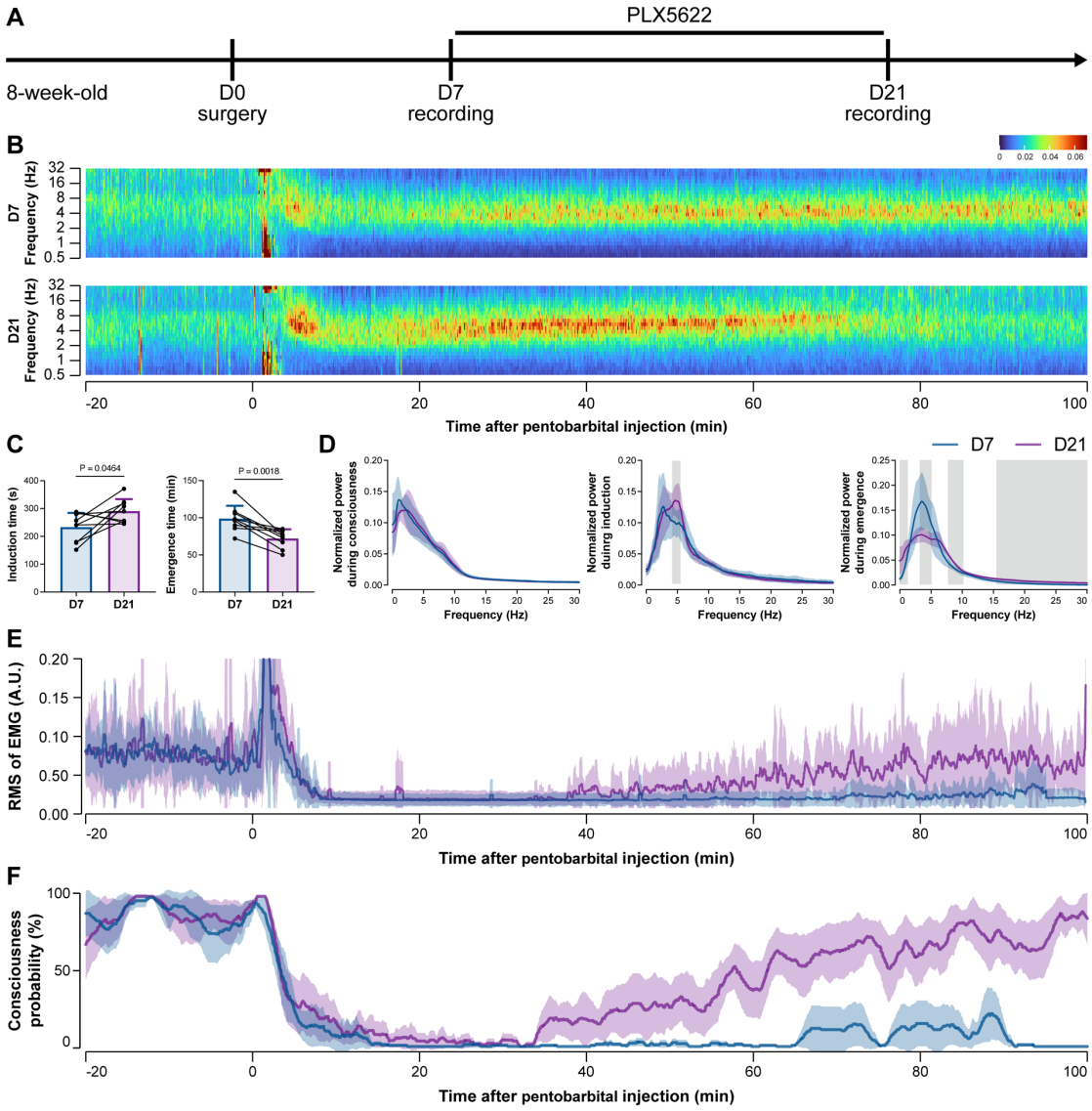

867

868 **Figure 4** EEG and EMG recordings reveal that mice with microglial depletion are
869 resistant to general anesthesia by pentobarbital.

870 **(A)** Scheme of time points for animal surgery, microglial depletion and EEG/EMG
871 recording.

872 **(B-D)** Microglial depletion shows no obvious change in EEG before the injection of
873 pentobarbital. Instead, it influences the EEG in anesthesia induction and emergence.
874 Two-tailed paired t test. The gray area in D indicates $P < 0.05$ between CD and
875 PLX5622.

876 **(E)** Microglial depletion does not change the EMG before the injection of pentobarbital.
877 Instead, it influences the EMG in the anesthesia process.

878 **(F)** Microglial depletion does not change the probability of consciousness before the

879 injection of pentobarbital. Instead, it influences the consciousness probability in the
880 anesthesia process.
881 N = 9 mice for each group. Data are presented as mean ± SD. RMS: root mean square;
882 A.U.: arbitrary unit; PLX5622: PLX5622-formulated diet.
883
884

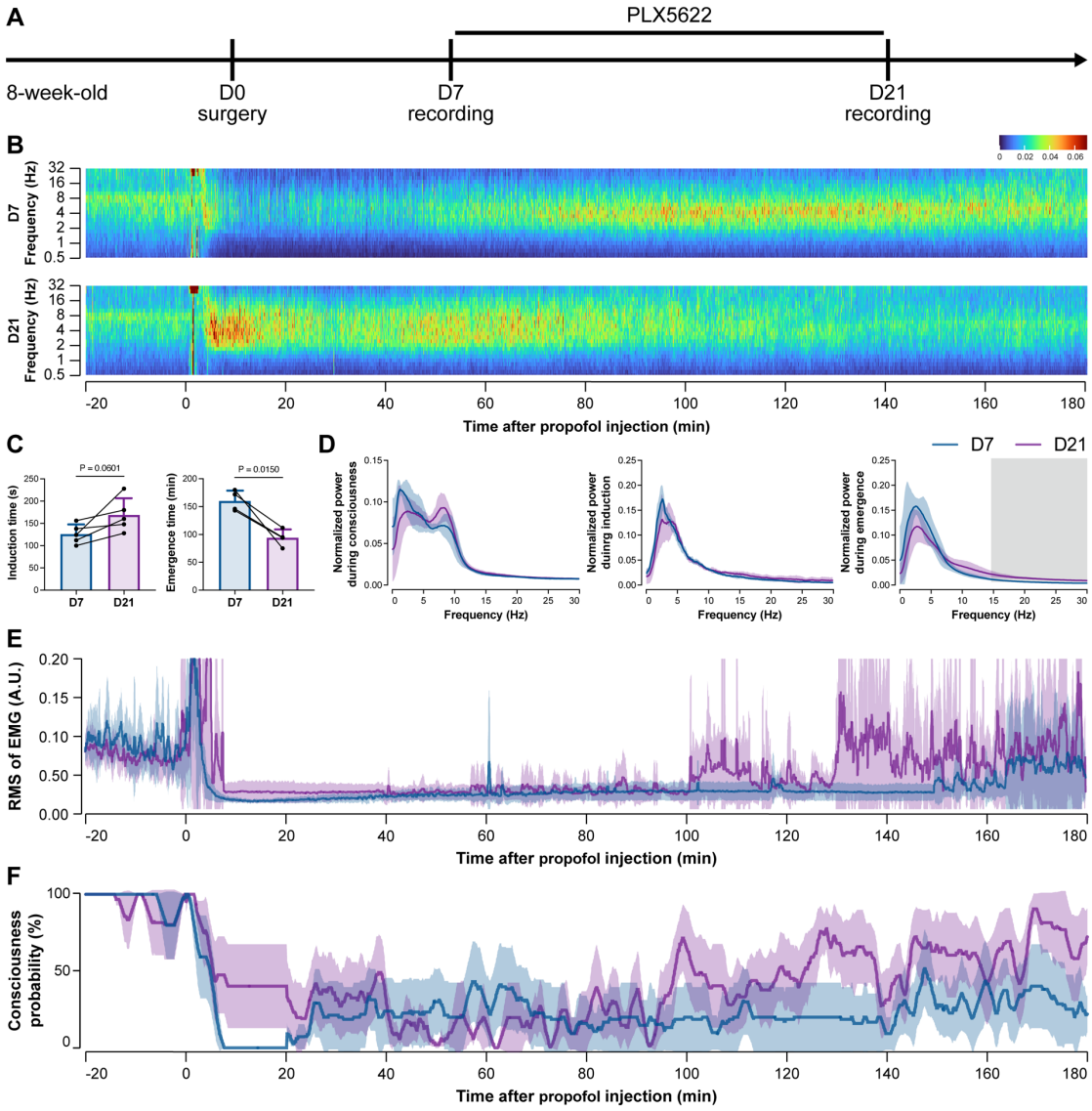

Figure 5 EEG and EMG recordings reveal that mice with microglial depletion are resistant to general anesthesia by propofol.

(A) Scheme of time points for animal surgery, microglial depletion and EEG/EMG recording.

(B-D) Microglial depletion does not change the EEG before the injection of propofol. Instead, it influences the EEG in anesthesia induction and emergence. Two-tailed paired t test. The gray area in D indicates $P < 0.05$ between CD and PLX5622.

(E) Microglial depletion does not change the EMG before the injection of propofol. Instead, it influences the EMG in the anesthesia process.

(F) Microglial depletion does not change the probability of consciousness before the injection of propofol. Instead, it influences the consciousness probability in the

anesthesia process.

N = 5 mice for each group. Data are presented as mean ± SD. RMS: root mean square; A.U.: arbitrary unit; PLX5622: PLX5622-formulated diet.

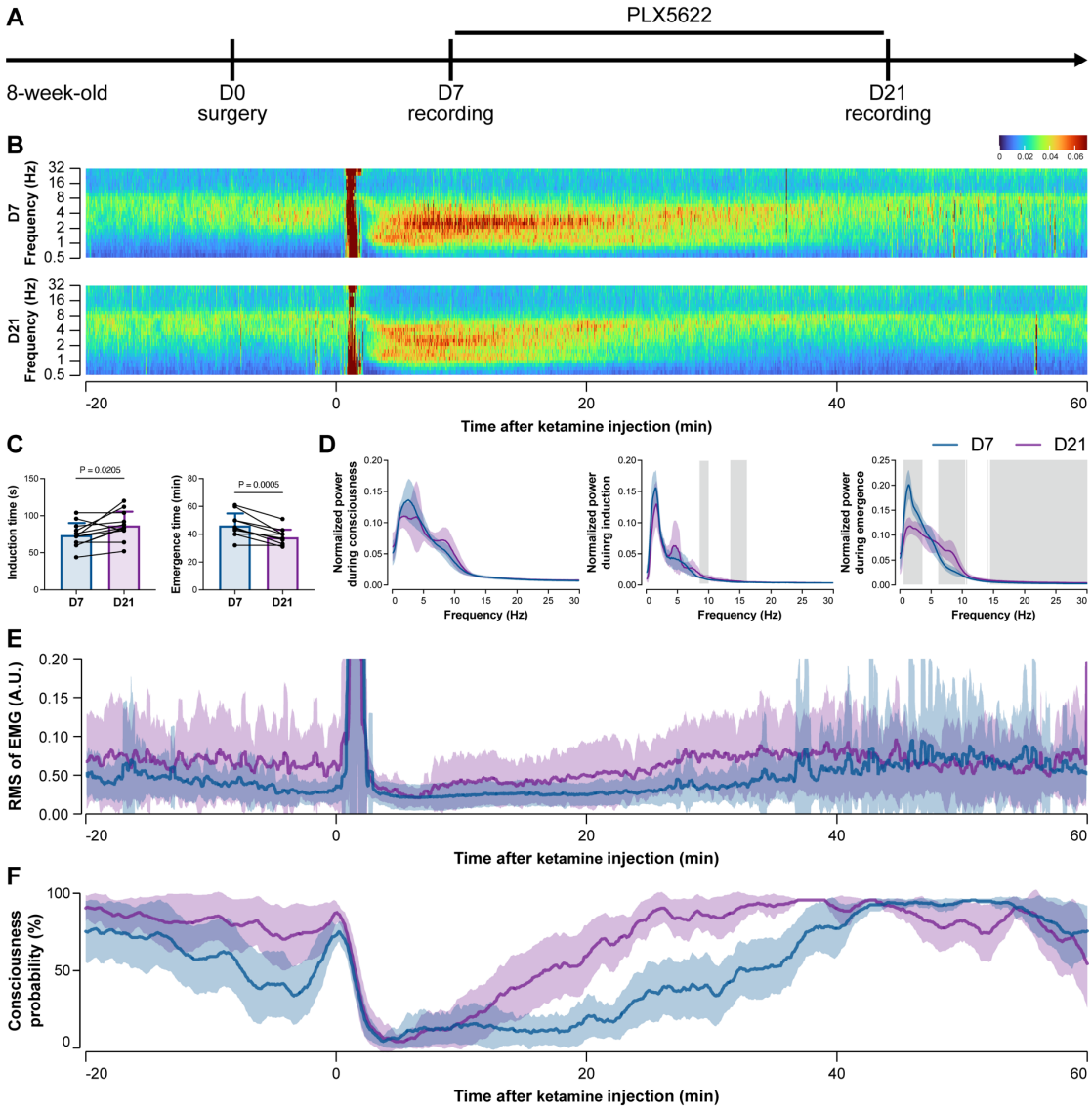

Figure 6 EEG and EMG recordings reveal that mice with microglial depletion are mouse resistant to general anesthesia by ketamine.

(A) Scheme of time points for animal surgery, microglial depletion and EEG/EMG recording.

(B-D) Microglial depletion does not change the EEG before the injection of ketamine. Instead, it influences the EEG in anesthesia induction and emergence. Two-tailed paired t test. The gray area in D indicates $P < 0.05$ between CD and PLX5622.

(E) Microglial depletion does not change the EMG before the injection of ketamine. Instead, it influences the EMG in the anesthesia process.

(F) Microglial depletion does not change the probability of consciousness before the injection of ketamine. Instead, it influences the consciousness probability in the

anesthesia process.

N = 12 mice for each group. Data are presented as mean ± SD. RMS: root mean square; A.U.: arbitrary unit; PLX5622: PLX5622-formulated diet.

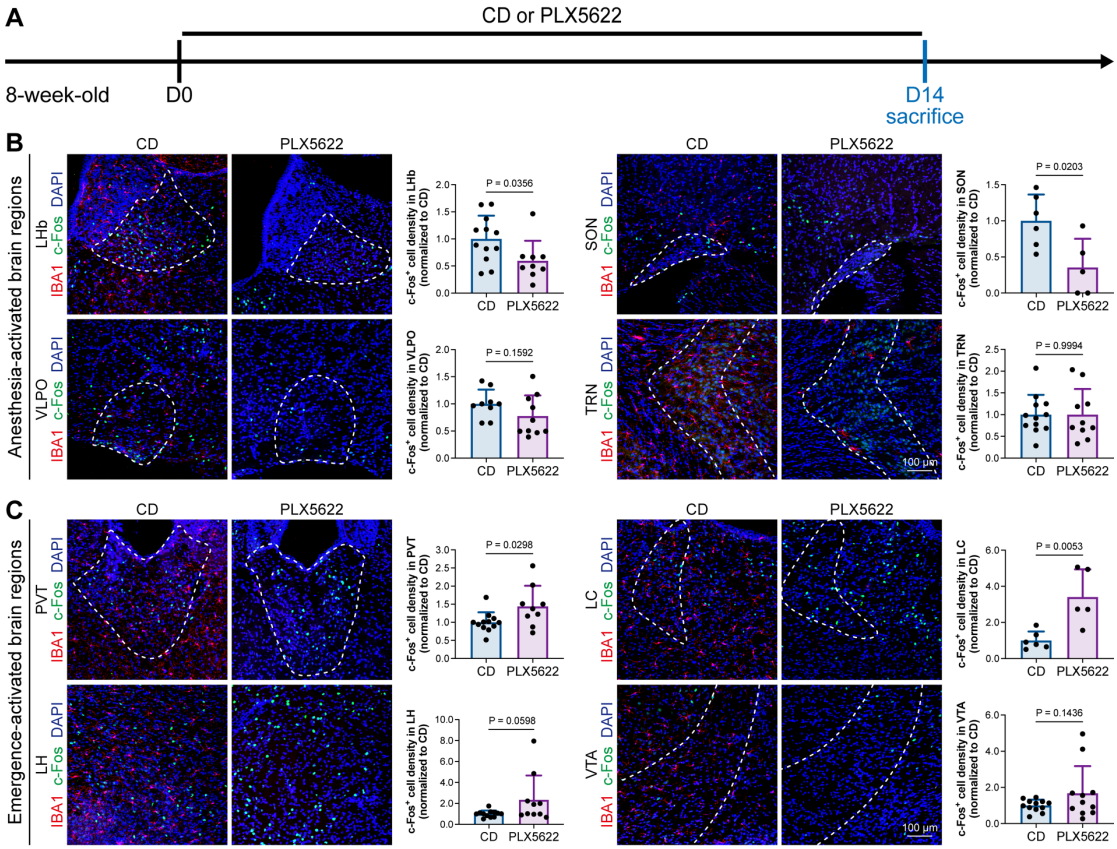

Figure 7 Microglial depletion diversely influences neuronal activity in different anesthesia-related brain regions.

(A) Scheme of time points for microglial depletion and examination time points.

(B) Influence of microglial depletion in anesthesia-activated brain regions. Microglial depletion reduces neuronal activity in the LHb (P = 0.0356), SON (P = 0.0203) and VLPO (P = 0.1592) and does not influence neuronal activity in the TRN (P = 0.9994). N = 12, 6, 9 and 12 mice for LHb, SON, VLPO and TRN in the CD group, respectively. N = 9, 5, 10 and 10 mice for LHb, SON, VLPO and TRN in the PLX5622 group, respectively.

(C) Influence of microglial depletion in emergence-activated brain regions. Microglial depletion enhances neuronal activity in the PVT (P = 0.0298), LC (P = 0.0053), LH (P = 0.0598) and VTA (P = 0.1436). N = 12, 6, 12 and 12 mice for PVT, LC, LH and VTA in the CD group, respectively. N = 9, 5, 10 and 11 mice for PVT, LC, LH and VTA in the PLX5622 group, respectively.

Two-tailed independent t test. Data are presented as mean ± SD. PLX5622: PLX5622-formulated diet; CD: control diet; LHb: lateral habenula; SON: supraoptic nucleus;

935 VLPO: ventrolateral preoptic nucleus; TRN: thalamic reticular nucleus; PVT:
936 paraventricular thalamus; LC: locus coeruleus; LH: lateral hypothalamus; VTA: ventral
937 tegmental area.
938

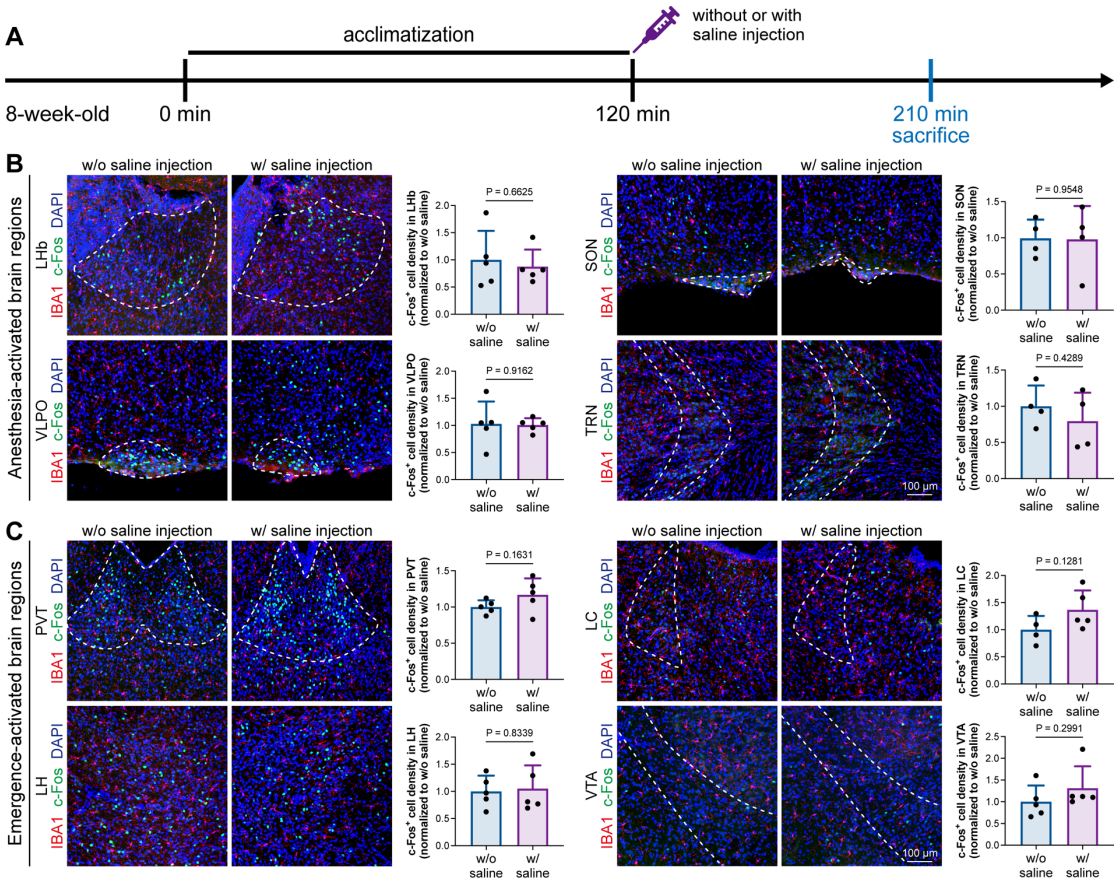

939

940 **Figure 8** Animal handling and intraperitoneal injection do not influence neuronal
941 activity in anesthesia-related brain regions.

942 **(A)** Scheme of time points for microglial depletion and examination time points.

943 **(B)** Microglial depletion does not influence neuronal activity in the LHb, SON, VLPO
944 or TRN. N = 5, 4, 5 and 4 mice for LHb, SON, VLPO and TRN in the CD group,
945 respectively. N = 5, 4, 5 and 4 mice for LHb, SON, VLPO and TRN in the PLX5622
946 group, respectively.

947 **(C)** Microglial depletion does not influence neuronal activity in the PVT, LC, LH or
948 VTA. N = 5, 4, 5 and 5 mice for PVT, LC, LH and VTA in the CD group, respectively.
949 N = 5, 5, 5 and 5 mice for PVT, LC, LH and VTA in the PLX5622 group, respectively.
950 Two-tailed independent t test. Data are presented as mean ± SD. PLX5622: PLX5622-
951 formulated diet; CD: control diet; LHb: lateral habenula; SON: supraoptic nucleus;
952 VLPO: ventrolateral preoptic nucleus; TRN: thalamic reticular nucleus; PVT:
953 paraventricular thalamus; LC: locus coeruleus; LH: lateral hypothalamus; VTA: ventral
954 tegmental area.

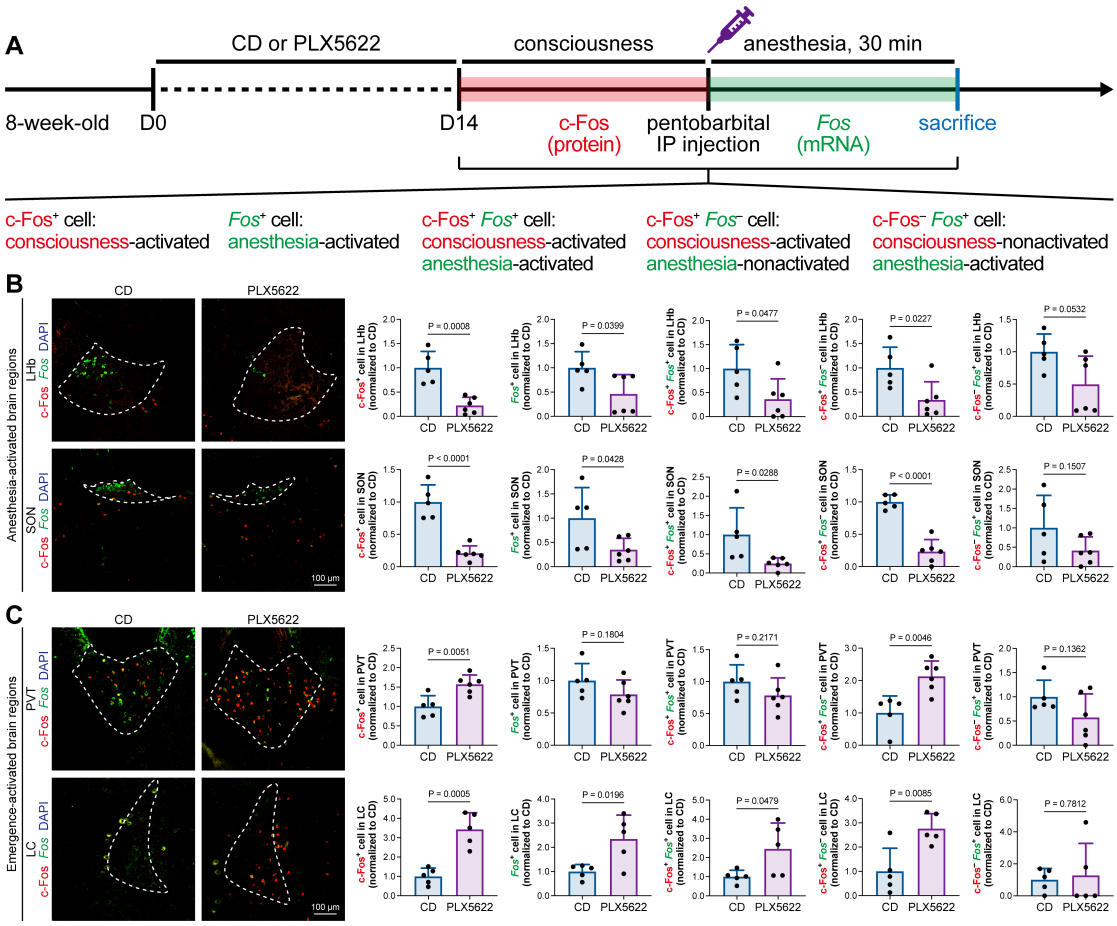

Figure 9 c-Fos protein and *Fos* mRNA dual staining dissects the influence of microglial depletion on consciousness and anesthesia states.

(A) Scheme of time points for microglial depletion and dual labeling.

(B-C) The influence of microglial depletion on activated neurons in consciousness and anesthesia states in AABRs (LHb and SON) and EABRs (PVT and LC). N = 5 (LHb CD), 6 (LHb PLX5622), 5 (SON CD), 6 (SON PLX5622), 5 (PVT CD), 6 (PVT PLX5622), 5 (LC CD) and 5 (LC PLX5622) mice for each group.

Two-tailed independent t test. Data are presented as mean ± SD. PLX5622: PLX5622-formulated diet; CD: control diet; LHb: lateral habenula; SON: supraoptic nucleus; PVT: paraventricular thalamus; LC: locus coeruleus.

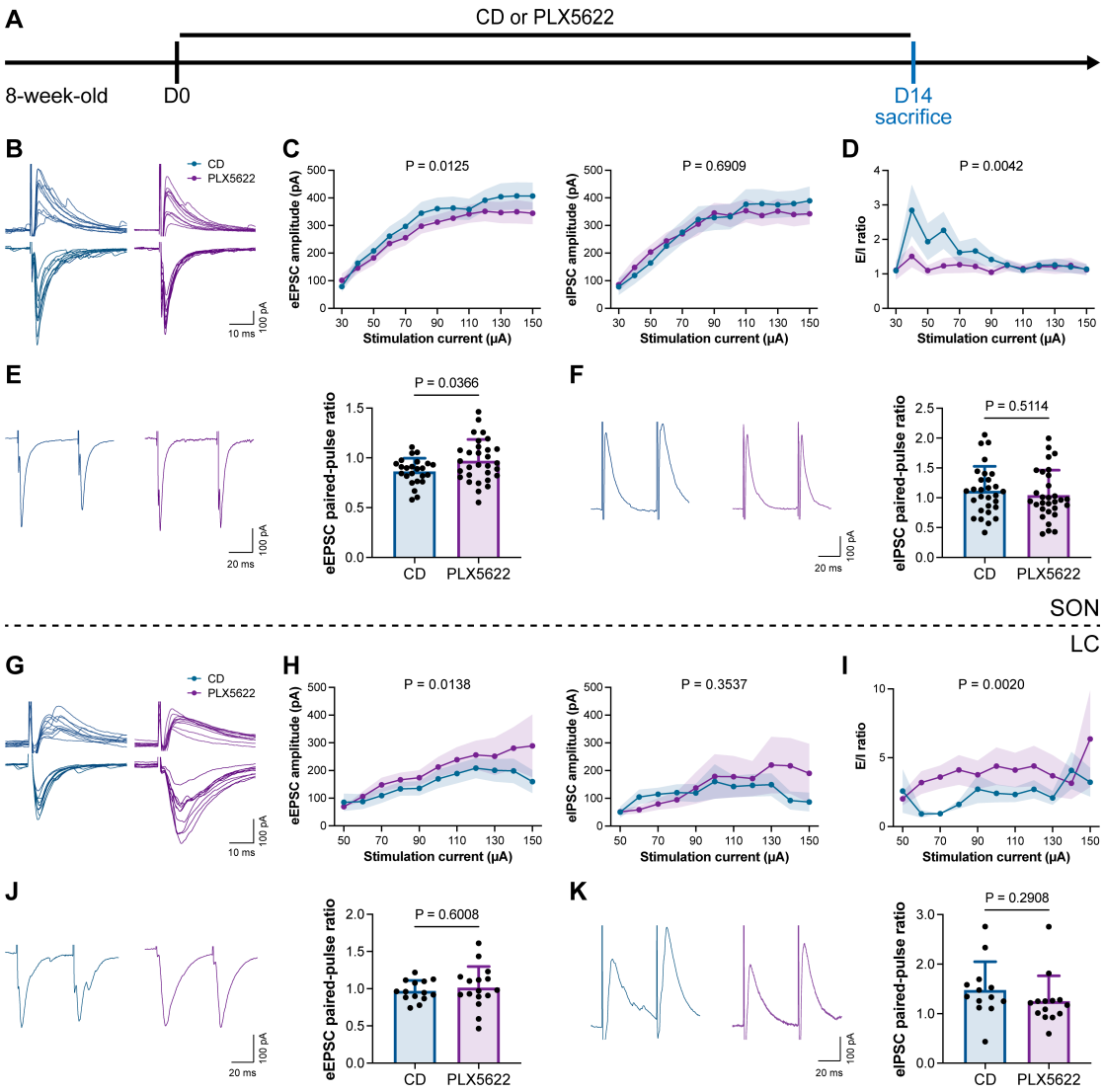

Figure 10 Microglial depletion reduces the E/I ratio in SON but enhances the E/I ratio in LC.

(A) Scheme of time points for microglial depletion by PLX5622.

(B) Representative traces for evoked postsynaptic currents in the SON to 10 increasing stimulation currents.

(C) Amplitudes of evoked postsynaptic currents in the SON in response to increasing electrical stimulation intensities. Two-way ANOVA. Data are presented as mean ± SEM.

(D) E/I ratios with different stimulation intensities in the SON. N = 21 cells from 5 mice for each group. Two-way ANOVA. Data are presented as mean ± SEM.

(E) Representative traces (left) and quantitative results (right) show that PLX5622-treated mice exhibited a higher eEPSC PPR in SON. N = 24 (CD) and 30 (PLX5622)

cells from 5 mice for each group. Two-tailed independent t test. Data are presented as mean ± SD.

(F) Representative traces (left) and quantitative results (right) show that PLX5622-treated mice exhibited a similar eIPSC PPR in SON. N = 29 (CD) and 30 (PLX5622) cells from 5 mice for each group. Two-tailed independent t test. Data are presented as mean ± SD.

(G) Representative traces for evoked postsynaptic currents in the LC in response to 10 increasing stimulation currents.

(H) Amplitudes of evoked postsynaptic currents in the LC in response to increasing electrical stimulation intensities. in response to the electrical stimulation. N = 15 (EPSC CD), 18 (EPSC PLX5622), 15 (IPSC CD) and 18 (IPSC PLX5622) cells from 5 mice for each group. Two-way ANOVA. Data are presented as mean ± SEM.

(I) E/I ratios with different stimulation currents in the LC. N = 15 (EPSC CD), 18 (EPSC PLX5622), 15 (IPSC CD) and 18 (IPSC PLX5622) cells from 5 mice for each group. Two-way ANOVA. Data are presented as mean ± SEM.

(J) Representative traces (left) and quantitative results (right) show that PLX5622-treated mice exhibited a similar eEPSC PPR in the LC. N = 14 (CD) and 16 (PLX5622) cells from 5 mice for each group. Two-tailed independent t test. Data are presented as mean ± SD.

(K) Representative traces (left) and quantitative results (right) show that PLX5622-treated mice exhibited a similar eIPSC PPR in the LC. N = 13 (CD) and 14 (PLX5622) cells from 5 mice for each group. Two-tailed independent t test. Data are presented as mean ± SD.

PLX5622: PLX5622-formulated diet; CD: control diet. eEPSC: evoked excitatory postsynaptic current; eIPSC: evoked inhibitory postsynaptic current.

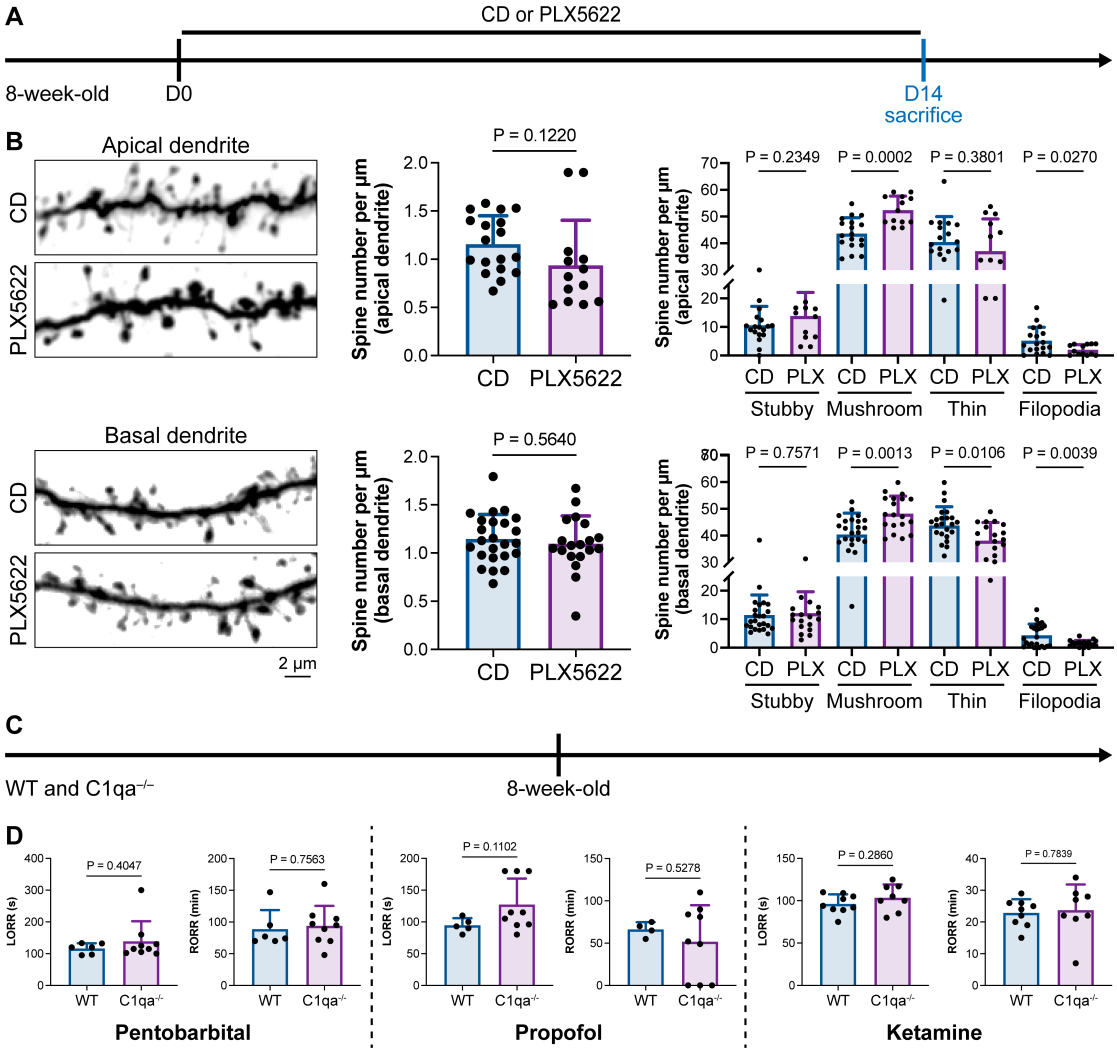

Figure 11 Interruption of the spine "eat me" signal by C1qa$^{-/-}$ does not influence the anesthesia process and microglial depletion alters the proportion of spine categories.

(A) Scheme of time points for microglial depletion and examination time points.

(B) CSF1R inhibition for 14 days does not influence spine density but changes the proportion of spine subtypes. N = 18 and 13 cells from 5 mice for each group of apical spines, N = 24 and 19 cells from 5 mice for each group of basal spines.

(C) Scheme of LORR and RORR tests in wild-type and C1qa$^{-/-}$ mice.

(D) C1q knockout does not influence anesthesia induction and emergence in response to pentobarbital, propofol and ketamine. N = 6 (pentobarbital WT), 9 (pentobarbital C1qa$^{-/-}$), 5 (propofol WT), 9 (propofol C1qa$^{-/-}$), 9 (ketamine WT) and 8 (ketamine C1qa$^{-/-}$).

Two-tailed independent t test. Data are presented as mean ± SD. PLX5622: PLX5622-formulated diet; CD: control diet; LORR: loss of righting reflex; RORR: recovery of righting reflex.

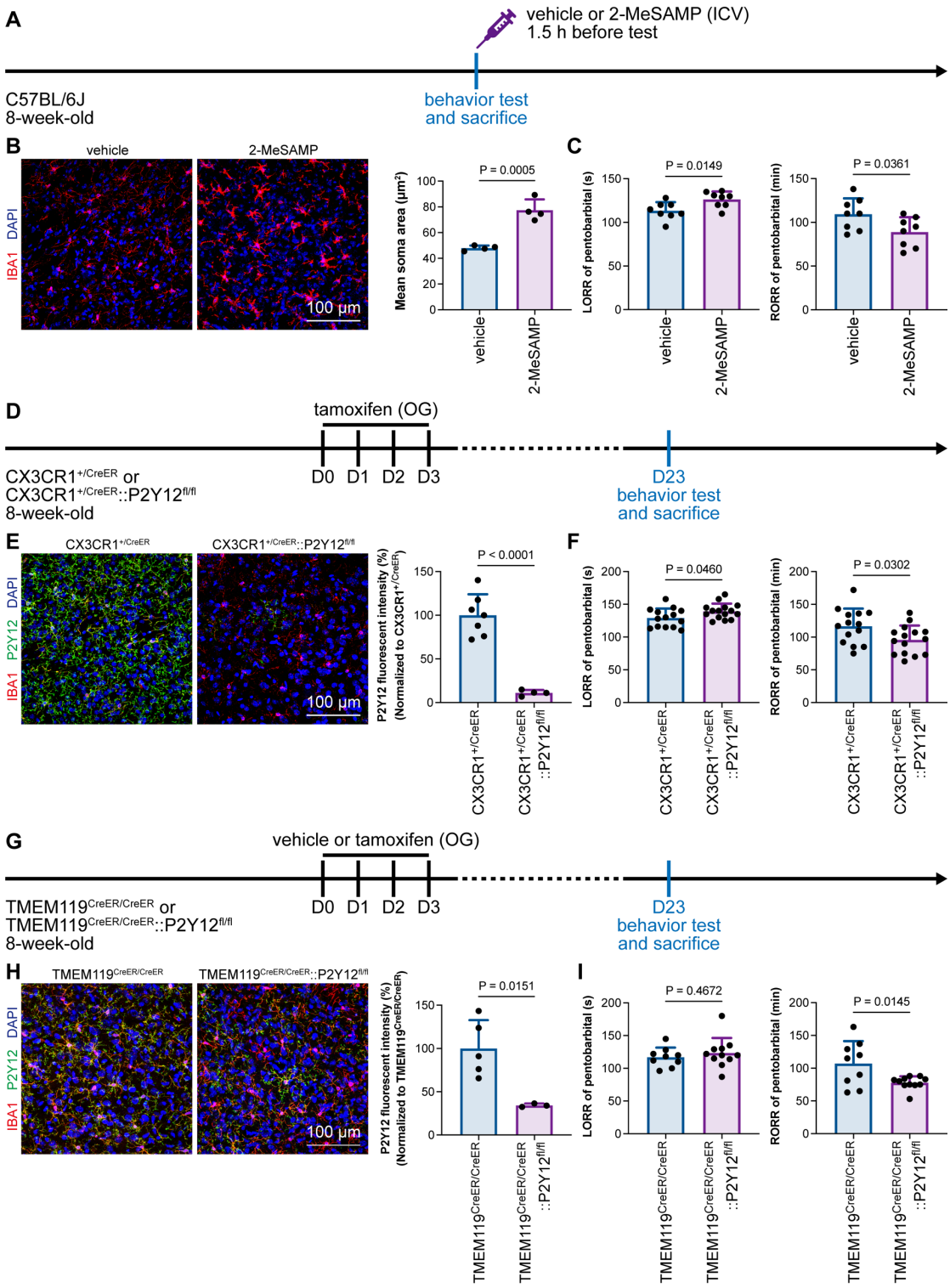

Figure 12 Microglial P2Y12 regulates the induction and emergence of anesthesia.

(A) Scheme of 2-MeSAMP administration and behavior tests for anesthesia.

(B) P2Y12 inhibition by 2-MeSAMP drives microglia to a more reactive state. N = 4 mice for each group.

(C) P2Y12 inhibition by 2-MeSAMP results in delayed anesthesia induction and early emergence. N = 8 mice for each group.

(D) Scheme of animal treatment and examination time points for $CX3CR1^{+/CreER}$ and $CX3CR1^{+/CreER}$::$P2Y12^{fl/fl}$ mice.

(E) Tamoxifen induces efficient P2Y12 knockout in $CX3CR1^{+/CreER}$::$P2Y12^{fl/fl}$ mice. N = 7 mice for the $CX3CR1^{+/CreER}$ group and 4 mice for the $CX3CR1^{+/CreER}$::$P2Y12^{fl/fl}$ group.

(F) Efficient knockout of P2Y12 significantly elongates the LORR and shortens the RORR. N = 14 mice for the $CX3CR1^{+/CreER}$ group and 15 mice for the $CX3CR1^{+/CreER}$::$P2Y12^{fl/fl}$ group.

(G) Scheme of animal treatment and examination time points for $TMEM119^{CreER/CreER}$ and $TMEM119^{CreER/CreER}$::$P2Y12^{fl/fl}$ mice.

(H) Tamoxifen induces relatively low efficiency of P2Y12 knockout in $TMEM119^{CreER/CreER}$::$P2Y12^{fl/fl}$ mice. N = 5 mice for the $TMEM119^{CreER/CreER}$ group and 3 mice for the $TMEM119^{CreER/CreER}$::$P2Y12^{fl/fl}$ group.

(I) Low-efficiency knockout of P2Y12 does not affect anesthesia induction but significantly shortens the emergence time. N = 9 mice for the $TMEM119^{CreER/CreER}$ group and 11 mice for the $TMEM119^{CreER/CreER}$::$P2Y12^{fl/fl}$ group.

Two-tailed independent t test. Data are presented as mean ± SD. ICV: intracerebroventricular; OG: oral gavage; LORR: loss of righting reflex; RORR: recovery of righting reflex.

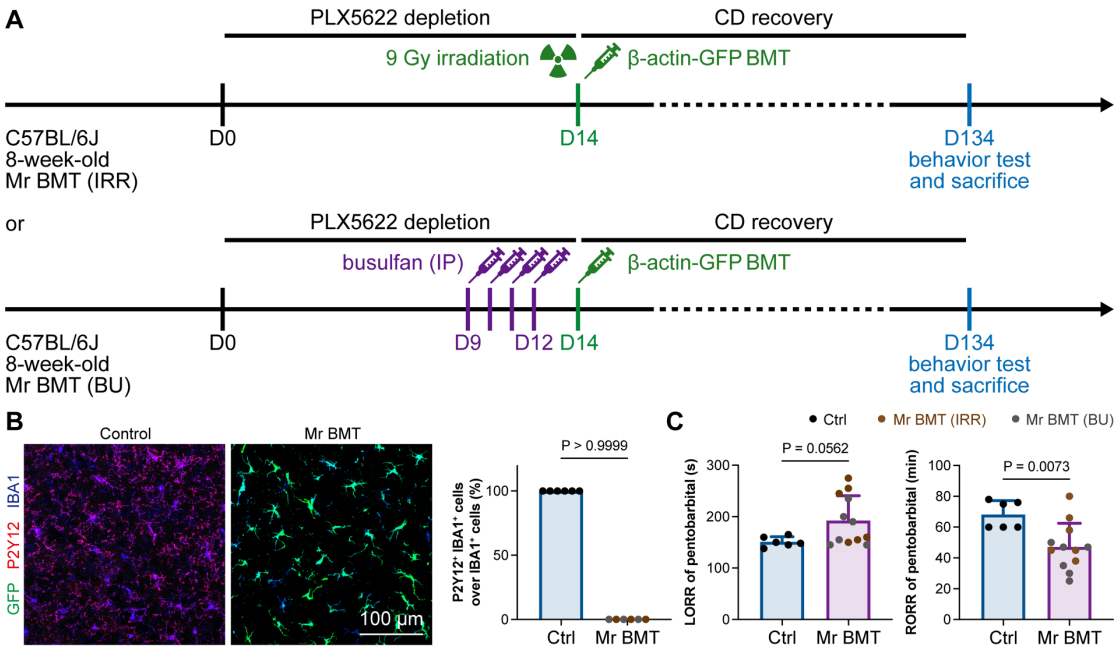

Figure 13 Mice with P2Y12⁻ Mr BMT cells display delayed anesthesia induction and early emergence.

(A) Scheme of microglia replacement by Mr BMT and behavior tests for anesthesia.

(B) Mr BMT cells exhibit a P2Y12⁻ phenotype. N = 6 mice for each group.

(C) P2Y12⁻ microglia lead to delayed anesthesia induction and early emergence. N = 6 mice for the control group, 6 mice for the Mr BMT (IRR) group and 6 mice for the Mr BMT (BU) group.

Two-tailed independent t test. Data are presented as mean ± SD. IP: intraperitoneal injection; Mr BMT: microglia replacement by bone marrow transplantation; BMT: bone marrow transplantation; Ctrl: control; IRR: irradiation; BU: busulfan; LORR: loss of righting reflex; RORR: recovery of righting reflex.

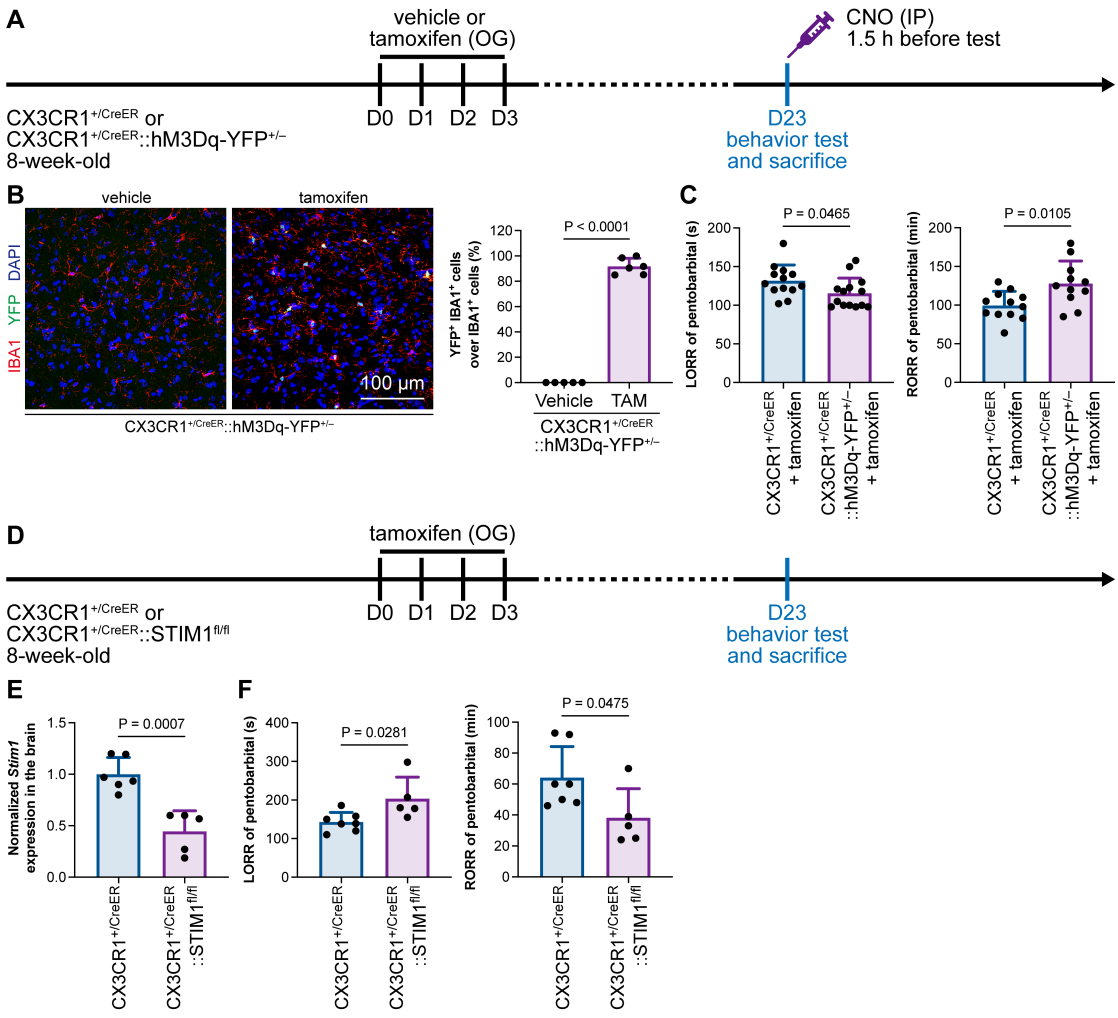

Figure 14 General anesthesia is regulated by intracellular calcium in microglia.

(A) Scheme of animal treatment and examination time points for CX3CR1$^{+/CreER}$ and CX3CR1$^{+/CreER}$::hM3Dq-YFP$^{+/–}$ mice.

(B) Tamoxifen induces high Cre-dependent recombination in CX3CR1$^{+/CreER}$::hM3Dq-YFP$^{+/–}$ mice. N = 5 mice for the vehicle group and 6 mice for the tamoxifen group.

(C) Elevation of microglial intracellular Ca^{2+} results in a shorter anesthesia induction time and longer emergence time. N = 13 (LORR CX3CR1$^{+/CreER}$), 14 (LORR CX3CR1$^{+/CreER}$::hM3Dq-YFP$^{+/–}$), 12 (RORR CX3CR1$^{+/CreER}$) and 11 (RORR CX3CR1$^{+/CreER}$::hM3Dq-YFP$^{+/–}$) mice per group.

(D) Scheme of animal treatment and examination time points for CX3CR1$^{+/CreER}$ and CX3CR1$^{+/CreER}$::STIM1$^{fl/fl}$ mice.

(E) qPCR results reveal decreased *Stim1* transcription in CX3CR1$^{+/CreER}$::STIM1$^{fl/fl}$ mouse brains. N = 6 mice for the CX3CR1$^{+/CreER}$ group and 5 mice for the CX3CR1$^{+/CreER}$::STIM1$^{fl/fl}$ group.

(F) Downregulation of microglial intracellular Ca^{2+} results in longer anesthesia induction time and shorter emergence time. N = 7 CX3CR1$^{+/CreER}$ and 5 CX3CR1$^{+/CreER}$::STIM1$^{fl/fl}$) mice per group.

Two-tailed independent t test. Data are presented as mean ± SD. OG: oral gavage; IP: intraperitoneal injection; TAM: tamoxifen; LORR: loss of righting reflex; RORR: recovery of righting reflex.

References

1. F. Ginhoux *et al.*, Fate mapping analysis reveals that adult microglia derive from primitive macrophages. *Science* **330**, 841-845 (2010).
2. S. Brioschi, Y. Zhou, M. Colonna, Brain Parenchymal and Extraparenchymal Macrophages in Development, Homeostasis, and Disease. *Journal of immunology* **204**, 294-305 (2020).
3. M. Prinz, S. Jung, J. Priller, Microglia Biology: One Century of Evolving Concepts. *Cell* **179**, 292-311 (2019).
4. Y. U. Liu *et al.*, Neuronal network activity controls microglial process surveillance in awake mice via norepinephrine signaling. *Nature neuroscience* 10.1038/s41593-019-0511-3 (2019).
5. R. D. Stowell *et al.*, Noradrenergic signaling in the wakeful state inhibits microglial surveillance and synaptic plasticity in the mouse visual cortex. *Nature neuroscience* 10.1038/s41593-019-0514-0 (2019).
6. A. D. Umpierre *et al.*, Microglial calcium signaling is attuned to neuronal activity in awake mice. *Elife* **9**, e56502 (2020).
7. G. O. Sipe *et al.*, Microglial P2Y12 is necessary for synaptic plasticity in mouse visual cortex. *Nature communications* **7**, 10905 (2016).
8. B. Stevens *et al.*, The classical complement cascade mediates CNS synapse elimination. *Cell* **131**, 1164-1178 (2007).
9. E. Favuzzi *et al.*, GABA-receptive microglia selectively sculpt developing inhibitory circuits. *Cell* 10.1016/j.cell.2021.06.018 (2021).
10. D. P. Schafer *et al.*, Microglia sculpt postnatal neural circuits in an activity and complement-dependent manner. *Neuron* **74**, 691-705 (2012).
11. U. B. Eyo, M. Murugan, L. J. Wu, Microglia-Neuron Communication in Epilepsy. *Glia* **65**, 5-18 (2017).
12. A. Badimon *et al.*, Negative feedback control of neuronal activity by microglia. *Nature* 10.1038/s41586-020-2777-8 (2020).
13. B. Erblich, L. Zhu, A. M. Etgen, K. Dobrenis, J. W. Pollard, Absence of colony stimulation factor-1 receptor results in loss of microglia, disrupted brain development and olfactory deficits. *PLoS One* **6**, e26317 (2011).
14. M. R. Elmore, R. J. Lee, B. L. West, K. N. Green, Characterizing newly repopulated microglia in the adult mouse: impacts on animal behavior, cell morphology, and neuroinflammation. *PLoS One* **10**, e0122912 (2015).
15. Y. Huang *et al.*, Dual extra-retinal origins of microglia in the model of retinal microglia repopulation. *Cell Discov* **4**, 9 (2018).
16. T. Zhou *et al.*, Microglial debris is cleared by astrocytes via C4b-facilitated phagocytosis and degraded via RUBICON-dependent noncanonical autophagy in mice. *Nature communications* **13**, 6233 (2022).
17. Y. Rao *et al.*, NeuroD1 induces microglial apoptosis and cannot induce microglia-to-neuron cross-lineage reprogramming. *Neuron* **109**, 4094-4108.e4095 (2021).
18. Z. Xu *et al.*, Efficient strategies for microglia replacement in the central nervous system. *Cell reports* **32**, 108041 (2020).
19. Y. Huang *et al.*, Repopulated microglia are solely derived from the proliferation of residual microglia after acute depletion. *Nature neuroscience* **21**, 530-540 (2018).

20. M. R. Elmore *et al.*, Colony-stimulating factor 1 receptor signaling is necessary for microglia viability, unmasking a microglia progenitor cell in the adult brain. *Neuron* **82**, 380-397 (2014).
21. C. N. Parkhurst *et al.*, Microglia promote learning-dependent synapse formation through brain-derived neurotrophic factor. *Cell* **155**, 1596-1609 (2013).
22. E. Spangenberg *et al.*, Sustained microglial depletion with CSF1R inhibitor impairs parenchymal plaque development in an Alzheimer's disease model. *Nature communications* **10**, 3758 (2019).
23. P. Jiang *et al.*, Nucleotide transmitters ATP and ADP mediate intercellular calcium wave communication via P2Y12/13 receptors among BV-2 microglia. *PLoS One* **12**, e0183114 (2017).
24. A. Jairaman *et al.*, TREM2 regulates purinergic receptor-mediated calcium signaling and motility in human iPSC-derived microglia. *Elife* **11** (2022).
25. A. Pozner *et al.*, Intracellular calcium dynamics in cortical microglia responding to focal laser injury in the PC::G5-tdT reporter mouse. *Frontiers in molecular neuroscience* **8**, 12 (2015).
26. K. Cao *et al.*, Microglia modulate general anesthesia through P2Y12 receptor. *Curr Biol* 10.1016/j.cub.2023.04.047 (2023).
27. X. Yang *et al.*, CSF1R blockade induces macrophage ablation and results in mouse choroidal vascular atrophy and RPE disorganization. *Elife* **9**, e55564 (2020).
28. T. C. Sykes, A. M. Thomson, Sodium pentobarbitone enhances responses of thalamic relay neurones to GABA in rat brain slices. *Br J Pharmacol* **97**, 1059-1066 (1989).
29. P. S. Sebel, J. D. Lowdon, Propofol: a new intravenous anesthetic. *Anesthesiology* **71**, 260-277 (1989).
30. D. M. Lovinger, S. A. Zimmerman, M. Levitin, M. V. Jones, N. L. Harrison, Trichloroethanol potentiates synaptic transmission mediated by gamma-aminobutyric acidA receptors in hippocampal neurons. *Journal of Pharmacology and Experimental Therapeutics* **264**, 1097-1103 (1993).
31. K. M. Garrett, J. Gan, Enhancement of gamma-aminobutyric acidA receptor activity by alpha-chloralose. *J Pharmacol Exp Ther* **285**, 680-686 (1998).
32. N. A. Anis, S. C. Berry, N. R. Burton, D. Lodge, The dissociative anaesthetics, ketamine and phencyclidine, selectively reduce excitation of central mammalian neurones by N-methyl-aspartate. *Br J Pharmacol* **79**, 565-575 (1983).
33. V. Bellver-Landete *et al.*, Microglia are an essential component of the neuroprotective scar that forms after spinal cord injury. *Nature communications* **10**, 518 (2019).
34. Q. Zhai *et al.*, Reducing complement activation during sleep deprivation yields cognitive improvement by dexmedetomidine. *Br J Anaesth* 10.1016/j.bja.2023.04.044 (2023).
35. C. Gelegen *et al.*, Excitatory Pathways from the Lateral Habenula Enable Propofol-Induced Sedation. *Curr Biol* **28**, 580-587 e585 (2018).
36. F. Zhou *et al.*, Orexinergic innervations at GABAergic neurons of the lateral habenula mediates the anesthetic potency of sevoflurane. *CNS Neurosci Ther* **29**, 1332-1344 (2023).
37. L. F. Jiang-Xie *et al.*, A Common Neuroendocrine Substrate for Diverse General Anesthetics and Sleep. *Neuron* **102**, 1053-1065 e1054 (2019).
38. L. E. Nelson *et al.*, The sedative component of anesthesia is mediated by GABA(A) receptors in an endogenous sleep pathway. *Nature neuroscience* **5**, 979-984 (2002).
39. Y. Zhang *et al.*, Activation of noradrenergic terminals in the reticular thalamus delays arousal from propofol anesthesia in mice. *FASEB journal : official publication of the Federation of*

American Societies for Experimental Biology **33**, 7252-7260 (2019).

40. Y. L. Wang *et al.*, Paraventricular thalamus controls consciousness transitions during propofol anaesthesia in mice. *Br J Anaesth* **130**, 698-708 (2023).
41. E. M. Vazey, G. Aston-Jones, Designer receptor manipulations reveal a role of the locus coeruleus noradrenergic system in isoflurane general anesthesia. *Proceedings of the National Academy of Sciences of the United States of America* **111**, 3859-3864 (2014).
42. A. Venner, C. Anaclet, R. Y. Broadhurst, C. B. Saper, P. M. Fuller, A Novel Population of Wake-Promoting GABAergic Neurons in the Ventral Lateral Hypothalamus. *Curr Biol* **26**, 2137-2143 (2016).
43. S. Zhao *et al.*, Lateral Hypothalamic Area Glutamatergic Neurons and Their Projections to the Lateral Habenula Modulate the Anesthetic Potency of Isoflurane in Mice. *Neuroscience bulletin* **37**, 934-946 (2021).
44. K. Solt *et al.*, Electrical stimulation of the ventral tegmental area induces reanimation from general anesthesia. *Anesthesiology* **121**, 311-319 (2014).
45. N. E. Taylor, J. J. Chemali, E. N. Brown, K. Solt, Activation of D1 dopamine receptors induces emergence from isoflurane general anesthesia. *Anesthesiology* **118**, 30-39 (2013).
46. J. Xiu *et al.*, Visualizing an emotional valence map in the limbic forebrain by TAI-FISH. *Nature neuroscience* **17**, 1552-1559 (2014).
47. H. Lui *et al.*, Progranulin Deficiency Promotes Circuit-Specific Synaptic Pruning by Microglia via Complement Activation. *Cell* **165**, 921-935 (2016).
48. R. C. Paolicelli *et al.*, Synaptic pruning by microglia is necessary for normal brain development. *Science* **333**, 1456-1458 (2011).
49. S. Rivest, A 'don't eat me' immune signal protects neuronal connections. *Nature* **563**, 42-43 (2018).
50. Y. Ma, A. Ramachandran, N. Ford, I. Parada, D. A. Prince, Remodeling of dendrites and spines in the C1q knockout model of genetic epilepsy. *Epilepsia* **54**, 1232-1239 (2013).
51. S. Srinivasan *et al.*, The P2Y12 antagonists, 2-methylthioadenosine 5'-monophosphate triethylammonium salt and cangrelor (ARC69931MX), can inhibit human platelet aggregation through a Gi-independent increase in cAMP levels. *The Journal of biological chemistry* **284**, 16108-16117 (2009).
52. P. Mastorakos *et al.*, Temporally distinct myeloid cell responses mediate damage and repair after cerebrovascular injury. *Nat Neurosci* **24**, 245-258 (2021).
53. A. Bedolla *et al.*, Finding the right tool: a comprehensive evaluation of microglial inducible cre mouse models. *bioRxiv* 10.1101/2023.04.17.536878, 2023.2004.2017.536878 (2023).
54. T. E. Faust *et al.*, A comparative analysis of microglial inducible Cre lines. *bioRxiv* 10.1101/2023.01.09.523268 (2023).
55. Z. Xu, X. Zhou, B. Peng, Y. Rao, Microglia replacement by bone marrow transplantation (Mr BMT) in the central nervous system of adult mice. *STAR Protoc* **2**, 100666 (2021).
56. B. L. Roth, DREADDs for Neuroscientists. *Neuron* **89**, 683-694 (2016).
57. D. J. Urban, B. L. Roth, DREADDs (designer receptors exclusively activated by designer drugs): chemogenetic tools with therapeutic utility. *Annual review of pharmacology and toxicology* **55**, 399-417 (2015).
58. M. Oh-Hora *et al.*, Dual functions for the endoplasmic reticulum calcium sensors STIM1 and STIM2 in T cell activation and tolerance. *Nature immunology* **9**, 432-443 (2008).

59. S. L. Zhang *et al.*, STIM1 is a Ca2+ sensor that activates CRAC channels and migrates from the Ca2+ store to the plasma membrane. *Nature* **437**, 902-905 (2005).
60. J. Stiber *et al.*, STIM1 signalling controls store-operated calcium entry required for development and contractile function in skeletal muscle. *Nature cell biology* **10**, 688-697 (2008).
61. F. Logiacco *et al.*, Microglia sense neuronal activity via GABA in the early postnatal hippocampus. *Cell reports* **37**, 110128 (2021).
62. L. Dissing-Olesen *et al.*, Activation of neuronal NMDA receptors triggers transient ATP-mediated microglial process outgrowth. *J Neurosci* **34**, 10511-10527 (2014).
63. Q. Bi *et al.*, Microglia-derived PDGFB promotes neuronal potassium currents to suppress basal sympathetic tonicity and limit hypertension. *Immunity* **55**, 1466-1482 e1469 (2022).
64. A. M. Klawonn *et al.*, Microglial activation elicits a negative affective state through prostaglandin-mediated modulation of striatal neurons. *Immunity* **54**, 225-234.e226 (2021).
65. Q. Li *et al.*, Developmental Heterogeneity of Microglia and Brain Myeloid Cells Revealed by Deep Single-Cell RNA Sequencing. *Neuron* **101**, 207-223.e210 (2019).
66. E. Császár *et al.*, Microglia modulate blood flow, neurovascular coupling, and hypoperfusion via purinergic actions. *J Exp Med* **219** (2022).
67. A. Badimon *et al.*, Negative feedback control of neuronal activity by microglia. *Nature* **586**, 417-423 (2020).
68. Y. J. Liu *et al.*, Research progress on adenosine in central nervous system diseases. *CNS Neurosci Ther* **25**, 899-910 (2019).
69. C. Wang *et al.*, Microglia mediate forgetting via complement-dependent synaptic elimination. *Science* **367**, 688-694 (2020).
70. Y. Chu *et al.*, Enhanced synaptic connectivity and epilepsy in C1q knockout mice. *Proc Natl Acad Sci U S A* **107**, 7975-7980 (2010).
71. M. Alves *et al.*, Expression and function of the metabotropic purinergic P2Y receptor family in experimental seizure models and patients with drug-refractory epilepsy. *Epilepsia* **58**, 1603-1614 (2017).
72. M. Mo *et al.*, Microglial P2Y12 Receptor Regulates Seizure-Induced Neurogenesis and Immature Neuronal Projections. *J Neurosci* **39**, 9453-9464 (2019).
73. L. van Olst *et al.*, Meningeal inflammation in multiple sclerosis induces phenotypic changes in cortical microglia that differentially associate with neurodegeneration. *Acta Neuropathol* **141**, 881-899 (2021).
74. Z. Xu, Y. Rao, B. Peng, Protocol for microglia replacement by peripheral blood (Mr PB). *STAR Protoc* **2**, 100613 (2021).
75. Z. Xu, B. Peng, Y. Rao, Microglia replacement by microglia transplantation (Mr MT) in the adult mouse brain. *STAR Protoc* **2**, 100665 (2021).
76. J. C. Lambert *et al.*, Meta-analysis of 74,046 individuals identifies 11 new susceptibility loci for Alzheimer's disease. *Nature genetics* **45**, 1452-1458 (2013).
77. T. Jonsson *et al.*, Variant of TREM2 associated with the risk of Alzheimer's disease. *N Engl J Med* **368**, 107-116 (2013).
78. R. Guerreiro *et al.*, TREM2 variants in Alzheimer's disease. *N Engl J Med* **368**, 117-127 (2013).
79. P. Yuan *et al.*, TREM2 Haplodeficiency in Mice and Humans Impairs the Microglia Barrier Function Leading to Decreased Amyloid Compaction and Severe Axonal Dystrophy. *Neuron* **92**, 252-264 (2016).

80. C. E. G. Leyns *et al.*, TREM2 function impedes tau seeding in neuritic plaques. *Nature neuroscience* 10.1038/s41593-019-0433-0 (2019).
81. L. Zhong *et al.*, Soluble TREM2 ameliorates pathological phenotypes by modulating microglial functions in an Alzheimer's disease model. *Nature communications* **10**, 1365 (2019).
82. S. Parhizkar *et al.*, Loss of TREM2 function increases amyloid seeding but reduces plaque-associated ApoE. *Nature neuroscience* 10.1038/s41593-018-0296-9 (2019).
83. F. L. Yeh, Y. Wang, I. Tom, L. C. Gonzalez, M. Sheng, TREM2 Binds to Apolipoproteins, Including APOE and CLU/APOJ, and Thereby Facilitates Uptake of Amyloid-Beta by Microglia. *Neuron* **91**, 328-340 (2016).
84. Y. Wang *et al.*, TREM2 lipid sensing sustains the microglial response in an Alzheimer's disease model. *Cell* **160**, 1061-1071 (2015).
85. Y. Rao, B. Peng, Allogenic microglia replacement: A novel therapeutic strategy for neurological disorders. *Fundamental Research* 10.1016/j.fmre.2023.02.025 (2023).
86. L. Zhang, Y. Wang, T. Liu, Y. Mao, B. Peng, Novel Microglia-based Therapeutic Approaches to Neurodegenerative Disorders. *Neuroscience bulletin* **39**, 491-502 (2023).
87. Y. Yoo, G. Neumayer, Y. Shibuya, M. Marc-Daniel Mader, M. Wernig, A cell therapy approach to restore microglial Trem2 function in a mouse model of Alzheimer's disease. *Cell stem cell* **30**, 1043-1053.e1046 (2023).
88. P. Jiang, M. Jin, Replacing microglia to treat Alzheimer's disease. *Cell stem cell* **30**, 1001-1003 (2023).
89. Y. Shibuya *et al.*, Treatment of a genetic brain disease by CNS-wide microglia replacement. *Science translational medicine* **14**, eabl9945 (2022).
90. H. Harz, P. Hegemann, Rhodopsin-regulated calcium currents in Chlamydomonas. *Nature* **351**, 489-491 (1991).
91. A. Bi *et al.*, Ectopic expression of a microbial-type rhodopsin restores visual responses in mice with photoreceptor degeneration. *Neuron* **50**, 23-33 (2006).
92. E. S. Boyden, F. Zhang, E. Bamberg, G. Nagel, K. Deisseroth, Millisecond-timescale, genetically targeted optical control of neural activity. *Nature neuroscience* **8**, 1263-1268 (2005).
93. F. Zhang *et al.*, Multimodal fast optical interrogation of neural circuitry. *Nature* **446**, 633-639 (2007).
94. G. M. Alexander *et al.*, Remote Control of Neuronal Activity in Transgenic Mice Expressing Evolved G Protein-Coupled Receptors. *Neuron* **63**, 27-39 (2009).
95. H. Zhu *et al.*, Chemogenetic Inactivation of Ventral Hippocampal Glutamatergic Neurons Disrupts Consolidation of Contextual Fear Memory. *Neuropsychopharmacology : official publication of the American College of Neuropsychopharmacology* **39**, 1880-1892 (2014).
96. T. Kaiser, G. Feng, Tmem119-EGFP and Tmem119-CreERT2 Transgenic Mice for Labeling and Manipulating Microglia. *eNeuro* **6** (2019).
97. S. Yona *et al.*, Fate mapping reveals origins and dynamics of monocytes and tissue macrophages under homeostasis. *Immunity* **38**, 79-91 (2013).
98. M. I. Fonseca *et al.*, Cell-specific deletion of C1qa identifies microglia as the dominant source of C1q in mouse brain. *Journal of neuroinflammation* **14**, 48 (2017).
99. M. Okabe, M. Ikawa, K. Kominami, T. Nakanishi, Y. Nishimune, 'Green mice' as a source of ubiquitous green cells. *FEBS letters* **407**, 313-319 (1997).
100. H. Zhu *et al.*, Cre-dependent DREADD (Designer Receptors Exclusively Activated by Designer

Drugs) mice. *Genesis* **54**, 439-446 (2016).

101. Y. Shi *et al.*, Microglia drive APOE-dependent neurodegeneration in a tauopathy mouse model. *J Exp Med* **216**, 2546-2561 (2019).

102. W. Binning *et al.*, Chronic hM3Dq signaling in microglia ameliorates neuroinflammation in male mice. *Brain Behav Immun* **88**, 791-801 (2020).

103. S. L. DeVos, T. M. Miller, Direct intraventricular delivery of drugs to the rodent central nervous system. *J Vis Exp* 10.3791/50326, e50326 (2013).

104. J. J. Glascock *et al.*, Delivery of therapeutic agents through intracerebroventricular (ICV) and intravenous (IV) injection in mice. *J Vis Exp* 10.3791/2968 (2011).

105. J. Y. Zhang *et al.*, Chronic Stress Remodels Synapses in an Amygdala Circuit-Specific Manner. *Biol Psychiatry* **85**, 189-201 (2019).

106. F. Niu *et al.*, The m6A reader YTHDF2 is a negative regulator for dendrite development and maintenance of retinal ganglion cells. *Elife* **11**, e75827 (2022).